

Gravitational waves from a compact star in a circular, inspiral orbit, in the equatorial plane of a massive, spinning black hole, as observed by LISA

Lee Samuel Finn

Department of Physics, Astronomy & Astrophysics, The Pennsylvania State University, University Park, Pennsylvania 16802

Kip S. Thorne

Theoretical Astrophysics, California Institute of Technology, Pasadena, California 91125

(Received 7 April 2000; revised manuscript received 1 August 2000; published 28 November 2000)

Results are presented from high-precision computations of the orbital evolution and emitted gravitational waves for a stellar-mass object spiraling into a massive black hole in a slowly shrinking, circular, equatorial orbit. The focus of these computations is inspiral near the innermost stable circular orbit (isco)—more particularly, on orbits for which the angular velocity Ω is $0.03 \lesssim \Omega/\Omega_{\text{isco}} \lesssim 1.0$. The computations are based on the Teuksolsky-Sasaki-Nakamura formalism, and the results are tabulated in a set of functions that are of order unity and represent relativistic corrections to low-orbital-velocity formulas. These tables can form a foundation for future design studies for the LISA space-based gravitational-wave mission. A first survey of applications to LISA is presented: Signal to noise ratios S/N are computed and graphed as functions of the time-evolving gravitational-wave frequency for the lowest three harmonics of the orbital period, and for various representative values of the hole's mass M and spin a and the inspiraling object's mass μ , with the distance to Earth chosen to be $r_o = 1$ Gpc. These S/N 's show a very strong dependence on the black-hole spin, as well as on M and μ . Graphs are presented showing the range of the $\{M, a, \mu\}$ parameter space, for which $S/N > 10$ at $r_o = 1$ Gpc during the last year of inspiral. The hole's spin a has a factor of ~ 10 influence on the range of M (at fixed μ) for which $S/N > 10$, and the presence or absence of a white-dwarf-binary background has a factor of ~ 3 influence. A comparison with predicted event rates shows strong promise for detecting these waves, but not beyond about 1 Gpc if the inspiraling object is a white dwarf or neutron star. This argues for a modest lowering of LISA's noise floor. A brief discussion is given of the prospects for extracting information from the observed waves.

PACS number(s): 04.30.Db, 04.80.Nn, 97.60.Lf

I. INTRODUCTION AND SUMMARY

Earth-based gravitational-wave detectors operate in the high-frequency band, $\sim 1-10^4$ Hz, in which lie the waves from black holes of masses $\sim (2-10^3)M_\odot$. Space-based detectors operate in the low-frequency band, $\sim 10^{-4}-1$ Hz, populated by waves from black holes of mass $\sim (10^3-10^8)M_\odot$. The high-frequency band is likely to be opened up early in the next decade by the Laser Interferometric Gravitational Wave Observatory—(LIGO)-VIRGO network of Earth-based detectors [1]. The premier instrument for the low-frequency band is the Laser Interferometer Space Antenna (LISA) [2].

The European Space Agency has selected LISA as one of three “Cornerstone” missions in its “Horizon 2000+” program, NASA has appointed a mission definition team for LISA, and ESA and NASA are negotiating with each other about the possibility of flying LISA as a joint ESA-NASA mission in the ~ 2010 time frame.

One of the most interesting and promising gravitational wave sources for LISA is the final epoch of inspiral of a compact, stellar-mass object into a massive black hole. In the LISA frequency band, where the central hole must have $M \lesssim 10^8 M_\odot$, all giant stars and main-sequence stars will be tidally disrupted before the end of their inspiral, but compact objects—white dwarfs, neutron stars, and small black holes—can survive intact. [Depending on the hole's spin, a

massive white dwarf will be disrupted before the end of inspiral if $M < M_{\text{max}} \sim (10^4-10^5)M_\odot$. Neutron stars and small black holes can never be tidally disrupted in the LISA frequency band.]

Sigurdsson and Rees [3] have estimated the event rate for such compact objects to spiral into massive black holes. “Assuming most spiral galaxies have a central black hole of modest mass ($\sim 10^6 M_\odot$) and a cuspy spheroid,” and for “very conservative estimates of the black hole masses and central galactic densities,” they estimate one inspiral per year within 1 Gpc distance of Earth. Most of the inspiraling objects are likely to be white dwarfs or neutron stars; the inspiral rate for stellar-mass black holes [$\mu \sim (6-10)M_\odot$] may be 10 times smaller, about 3 per year out to 3 Gpc, according to Sigurdsson [4]. Sigurdsson notes, however, that the evidence for a recent burst of star formation in the central region of our galaxy suggests that normal nucleated spirals might have such starbursts every $\sim 10^8$ y, which would enhance the stellar-mass black-hole density by a factor of ~ 10 and would lead to stellar-mass black-hole inspirals of one per year out to 1 Gpc. He notes, further, that if there was just one $50M_\odot$ black hole in the core of each galaxy now containing a $\sim 10^6 M_\odot$ central black hole, the result would be several inspirals of such $50M_\odot$ holes per year out to a cosmological redshift $z=1$, all readily observable by LISA.

LISA's observations of waves from such inspirals will have major scientific payoffs [5]:

(i) Ryan [6] has shown that for circular equatorial orbits, the waves will carry, encoded in themselves, a map of the vacuum spacetime metric of the central black hole (or, equivalently, the values of the hole’s multiple moments), and he has made a first, very crude, estimate of the precision with which LISA can extract that map [7]. Ryan’s estimate is quite promising. From the extracted map, one can determine whether the hole’s geometry is that of the Kerr metric (i.e. “test the black-hole no hair theorem”), and one can use such maps to search for other kinds of conjectured massive central bodies (e.g. soliton stars [8] and naked singularities). It seems likely that this is true not only for circular geodesic orbits, but also for generic orbits.

(ii) The observation of many such events will provide (i) a census of the masses and spins of the massive central holes, (ii) a census of the masses of the inspiraling objects (which depend on and thus tell us about the initial stellar mass function and mass segregation in the central parsec of galactic nuclei), and (iii) a census of event rates (which depend on physical processes and on gravitational potentials in the central parsec).

(iii) In active galactic nuclei, the inspiral orbit may be significantly affected by drag in an accretion disk, producing both complications in the interpretation of the observations and opportunities for learning about the disks’ mass distribution [9].

In planning for the LISA mission, it is important to understand the details of the waves emitted by such inspirals. Those details are the most important factors in the choice of the mission’s noise floor and its duration, and are likely to be the principal drivers of its data analysis requirements and algorithms.

The foundations for computing the emitted waves are nearly all in place:

(i) If the orbit is known, then the waveforms and strengths can be computed using the Teukolsky- [10] Sasaki-Nakamura [11] (TSN) formalism for first-order perturbations of Kerr black holes.

(ii) The orbital evolution is governed by radiation reaction (and, if there is a robust accretion disk present, by accretion-disk drag [9]). Most massive holes are in galaxies with normal (non-active) nuclei, and are thought to be surrounded by tenuous disks with “advection-dominated accretion flow” (ADAF). Narayan [12] has shown that accretion drag should be totally negligible in such ADAF disks, so the orbital evolution is very cleanly governed by radiation reaction. This is the situation that we analyze in this paper; we ignore accretion-disk drag. Those few holes that are in active galactic nuclei may be surrounded by “thin” or “slim” accretion disks, for which Chakrabarti and colleagues [9] have shown that accretion-disk drag may be significant.

(iii) The radiation reaction’s influence on the orbit can be characterized fully by the rates of change of three “constants” of the orbital motion: the orbital energy E , axial component of angular momentum L , and Carter constant Q [13]. From the emitted waves (computed via the TSN formalism), one can read off $\dot{E} \equiv dE/dt$ and \dot{L} , but the only

known way to compute \dot{Q} is directly from the radiation reaction force.

(iv) A formal expression for the radiation reaction force has been derived recently by Mino *et al.* [14] and by Quinn and Wald [15], and several researchers are now working hard to convert this into a practical computational tool for deducing \dot{Q} [16]. This will complete the necessary set of tools for computing all details of the emitted waves.

The emitted waves will be so complex and so rich in structure and in parameter dependence, that it will require extensive computations to give us the full knowledge required by the LISA mission. Those computations are proceeding in stages:

(1) Initial quick surveys, based on the Newtonian or quasi-Newtonian orbits and the quadrupole-moment approximation to gravitational-wave emission. Such surveys are the foundation for the event rate estimates by Sigurdsson and Rees discussed above.

(2) More detailed and accurate surveys for orbits in the massive hole’s equatorial plane, using the TSN formalism. Such surveys do not require computing \dot{Q} , since Q vanishes for equatorial orbits. These surveys are of several types:

(a) Studies of the evolution of the orbit’s eccentricity. Such studies have been carried out by Tanaka and co-workers [17,18] and Cutler *et al.* [19] for non-spinning holes, and by Kennefick [20] for small eccentricities around spinning holes. These studies, coupled with estimates of the orbital eccentricities when the objects are far from the hole and are being frequently perturbed by near encounters with other objects [21,3], suggest that, despite the circularizing effect of radiation reaction, the eccentricities will still typically be large, $e \gtrsim 0.3$, when the object nears the hole’s horizon.

(b) Systematic computations of the details of the emitted waves and the orbital evolution for circular, equatorial orbits. This paper presents such computations and a companion paper [22] extends them to the *transition regime*, near the innermost stable circular orbit (isco), during which the orbit makes a gradual transition from adiabatic inspiral to a plunge into the hole.

(c) Computations of the waves’ details and orbital evolution for elliptic, equatorial orbits. First explorations have been carried out by Shibata for general ellipticity [23] and by Kennefick for small ellipticity [20] (though in the 1970s and 1980s there were studies for equatorial orbits that plunge from radial infinity into a hole or scatter off a hole [24]).

(3) Surveys of the orbital evolution and waves for circular orbits out of the hole’s equatorial plane. It is known that radiation reaction drives circular orbits into circular orbits, thereby causing \dot{Q} to evolve in a manner that is fully determined by TSN-formalism calculations of \dot{E} and \dot{Q} [25–27]. Therefore, the tools are fully in hand for these surveys, and Hughes [28] is in the late stages of the first one. (See Shibata [29] for an exploration of the wave emission before anyone knew how, correctly, to compute the orbital evolution, and see Shibata *et al.* [30] for studies of orbits with very small inclination angles to the equatorial plane.)

(4) Surveys of orbital evolution and waves for the generic, most realistic situation: elliptic orbits outside the equatorial

plane. Such surveys must await a practical computation technique for \dot{Q} .

For circular, equatorial orbits (the subject of this paper), there have been extensive previous calculations, beginning with the pioneering study by Detweiler [31]; for a review see Mino *et al.* [18]. However, these previous calculations have been motivated by the needs of LIGO-VIRGO observations in the high-frequency band, where (i) the ratio μ/M of object mass to hole mass is not very small, so finite-mass-ratio effects (omitted by the TSN formalism) are important, and (ii) almost all of the observed inspiral signal comes from radii large compared to the hole's horizon, so post-Newtonian techniques can be used. The previous calculations have focused almost entirely on carrying the post-Newtonian calculations to very high order, on developing techniques for accelerating their convergence, and—via comparison with TSN calculations—on evaluating their convergence [18].

LISA's regime and needs are quite different from this. For LISA, most of the signals are likely to come from systems with extreme mass ratios, $\mu/M \ll 1$, for which (a) the TSN formalism is highly accurate and (b) the object lingers for a very long time in the vicinity of the hole's horizon before plunging into it. This means that post-Newtonian calculations are neither needed, nor appropriate.

Because of these differences between the LIGO-VIRGO regime and the LISA regime, the previous TSN-based studies do not serve LISA's needs. The purpose of this paper is to begin filling that gap, specifically, the following:

In this paper we introduce a new set of functions \mathcal{N} , \mathcal{T} , $\dot{\mathcal{E}}$, to characterize the orbital evolution and the emitted waves. These functions are dimensionless and of order unity, and depend on the hole's dimensionless spin parameter $a = (\text{angular momentum})/M^2$ and on the orbit's dimensionless radius $\tilde{r} = r/M$. We give extensive tables of these functions, as computed using the TSN formalism. We then use those tables to compute the evolution of the waves' frequency and signal strength in LISA for a number of instructive values of the parameters $M = (\text{hole mass})$, $a = (\text{hole spin parameter})$, $\mu = (\text{object mass})$, and $m = (\text{wave harmonic order}) \equiv (\text{wave frequency})/(\text{orbital frequency})$. From these computations we draw a number of conclusions of importance for the LISA mission.

The paper is organized as follows. Our notation, including the dimensionless functions \mathcal{N} , \mathcal{T} , . . . , is introduced in Sec. II. Formulas for computing the dimensionless functions, and formulas for the orbital evolution and the waves' properties are given in Sec. III. Tables of the dimensionless functions are given and discussed in Sec. IV. Applications to LISA are presented in Sec. V. Finally, concluding remarks are given in Sec. VI.

II. NOTATION

In this paper we shall adopt the following notation to describe the compact object's inspiral and the gravitational waves it emits; throughout we use geometrized units; i.e., we set $G \equiv (\text{Newton's gravitation constant}) = 1$ and $c \equiv (\text{speed of light}) = 1$.

μ : the mass of the inspiraling object.

M : the black hole's mass.

$\eta \equiv \mu/M$: the mass ratio, assumed $\ll 1$.

$a \equiv S/M^2$: the hole's "rotation parameter"; here S is the hole's spin angular momentum.

r : the orbit's Boyer-Lindquist radial coordinate, defined by $\sqrt{r^2 + a^2}(1 + 2M/r) = (1/2\pi) \times (\text{the object's orbital circumference})$.

\tilde{r} : a tilde over a quantity means that it has been made dimensionless by multiplying by the appropriate power of M and, when the quantity is $\propto \mu$, multiplying by a factor $1/\mu$.

$\tilde{r} \equiv r/M$: the dimensionless radius of the orbit.

Ω : the object's orbital angular velocity, as measured using Boyer-Lindquist coordinate time t (defined below), i.e., using clocks that are far from the hole and at rest with respect to it.

$\tilde{\Omega} \equiv M\Omega$: the dimensionless orbital angular velocity, which is related to \tilde{r} by $\tilde{\Omega} = 1/(\tilde{r}^{3/2} + a)$; cf. Eq. (2.16) of Ref. [32]. When $\tilde{\Omega}$ is small (large \tilde{r}), Kepler's laws dictate that $\tilde{\Omega} \approx (M/r)^{3/2} = (\text{orbital velocity})^3$, i.e. $(\text{orbital velocity}) \approx \Omega^{1/3}$.

Subscript isco: a quantity evaluated at the object's innermost stable circular orbit ("isco"), where the inspiral ends and the plunge begins; for example, $\tilde{\Omega}_{\text{isco}}$ is the value of $\tilde{\Omega}$ at the isco.

t : Boyer-Lindquist coordinate time or, equivalently, time as measured at "radial infinity" or on Earth.

T : the Boyer-Lindquist time Δt until the isco is reached, i.e. the total remaining duration of the inspiral.

N_{orb} : the number of orbits remaining until the isco is reached.

r_o : the distance from the binary to Earth.

m : the order of a harmonic of the orbital frequency.

$f_m = (m/2\pi)\Omega$: the frequency of gravitational waves in the m th harmonic.

E : the object's total energy including rest mass, i.e., the component $-p_t$ of its 4-momentum. Note that, because the object is gravitationally bound to the black hole, $E < \mu$, its gravitational binding energy is $\mu - E > 0$.

$\tilde{E} \equiv E/\mu$.

\dot{E}_∞ : the total rate of emission of energy into gravitational waves that go to infinity.

\dot{E}_H : the total rate of emission of energy into gravitational waves that go down the horizon.

$\dot{E}_{\text{GW}} \equiv \dot{E}_\infty + \dot{E}_H$: the total rate of emission of energy into gravitational waves that go both to infinity and down the hole's horizon, and also, by energy conservation, the rate of decrease of the object's total energy; i.e., $\dot{E}_{\text{GW}} \equiv dE_{\text{GW}}/dt = -dE/dt$.

$\dot{E}_{\infty m}$: the total rate of emission of energy into the m th harmonic of the waves that go to infinity.

$h_{o,m} \equiv \sqrt{\langle h_{m+}^2 + h_{m\times}^2 \rangle}$: the *rms amplitude* of the gravitational waves in harmonic m emitted toward infinity, at a time when the wave frequency is f_m ; here $h_{m+}(t, \mathbf{n})$ and $h_{m\times}(t, \mathbf{n})$ are the two waveforms emitted in a direction \mathbf{n} and arriving at the Earth's distance r_o ; $\langle \dots \rangle$ is an average over

\mathbf{n} and over a period of the waves, and the average over time automatically produces a factor 1/2 thereby making $h_{o,m}^2$ be the mean value of $\frac{1}{2}[(\text{amplitude of } h_{m+})^2 + (\text{amplitude of } h_{m,\times})^2]$.

$h_{c,m} \equiv h_{o,m} \sqrt{2f_m^2/\dot{f}_m}$: a *characteristic amplitude* for the waves in harmonic m ; here and throughout this paper the overdot denotes a time derivative. The significance of $h_{c,m}$ is discussed below.

$h'_{c,m} \equiv h_{c,m} \min[1, \sqrt{3(1-f_m/f_{m,\text{isco}})}]$: A modified characteristic amplitude, discussed below.

$h_n(f) \equiv \sqrt{f} S_h^{\text{SA}}(f)$: LISA's "sky-averaged" rms noise in a bandwidth equal to frequency f . Here $S_h^{\text{SA}}(f)$ is the one-sided spectral density $S_{h_+}(f)$ for some linear polarization $+$, inverse averaged over source directions and polarization ("sky-averaged"), $1/S_h^{\text{SA}} \equiv \langle 1/S_{h_+} \rangle$.

From the general relation $dE_{\text{GW}}/dt dA = (1/16\pi)(\dot{h}_+^2 + \dot{h}_\times^2)$ for the energy flux in gravitational waves in terms of the time derivatives of the two waveforms [Eq. (10) of Ref. [33]], we infer that the rms amplitude and the energy in harmonic m are related to each other by

$$h_{o,m} = \frac{2\sqrt{\dot{E}_{\infty m}}}{m\Omega r_o}. \quad (2.1)$$

We shall use, as our measure of where the object is in its orbit, the dimensionless orbital angular frequency $\tilde{\Omega}$, which is related to the gravitational-wave frequency in harmonic m by $f_m = (m/2\pi M)\tilde{\Omega}$. We shall write various fully relativistic, time-evolving quantities (\dot{E}_{GW} , $h_{c,m}$, etc.) as the leading-order ("Newtonian") term in an expansion in $\tilde{\Omega}^{1/3} \simeq (\text{orbital velocity})$, multiplied by relativistic corrections. Our notation for the relativistic corrections will be the following:

\mathcal{N} : the correction to $\Omega^2/\dot{\Omega} \equiv \tilde{\Omega}^2/\dot{\tilde{\Omega}}$, where the overdot is a time derivative. Note that $\Omega^2/\dot{\Omega} = d\Phi/d\ln\Omega$ is the number of radians $d\Phi$ of orbital motion required to produce (due to radiation reaction) a fractional change $d\Omega/\Omega$ in the orbital frequency.

\mathcal{N}_{orb} : the correction to N_{orb} (the number of orbits remaining until the end of the inspiral).

\mathcal{T} : the correction to T (the remaining time to the end of the inspiral).

$\dot{\mathcal{E}}$: the correction to \dot{E}_{GW} (the total energy loss rate).

$\dot{\mathcal{E}}_{\infty m}$: the correction to $\dot{E}_{\infty m}$ (the energy radiated to infinity in harmonic m).

$\mathcal{H}_{o,m}$: the correction to $h_{o,m}$ (the rms wave amplitude in harmonic m).

$\mathcal{H}_{c,m}$: the correction to $h_{c,m}$ (the characteristic amplitude in harmonic m).

The *characteristic amplitude* $h_{c,m}$ needs some explanation. As the object spirals inward in its orbit, its m th harmonic waves spend $\sim f_m^2/\dot{f}_m = d\Phi_m/(2\pi d\ln f_m)$ cycles in the vicinity of frequency f_m (where Φ_m is the harmonic's phase). Correspondingly, in a detector that observes the waves throughout the inspiral epoch $\Delta t = f_m/\dot{f}_m$, the signal

is enhanced, in comparison to the detector noise, by approximately the square root of this quantity. The signal strength is thus approximately the same as would be produced by a broad-band burst of amplitude $h_{c,m} \equiv h_{o,m} \sqrt{2f_m^2/\dot{f}_m}$.

The factor of 2 inside the square root arises from a more precise definition of $h_{c,m}$ [34]: The signal to noise ratio produced by the waves' m th harmonic, averaged over all possible orientations of the source and the detector, is given by

$$\left(\frac{S}{N}\right)_{\text{rms}} = \sqrt{\int \left[\frac{h_{c,m}(f_m)}{h_n(f_m)}\right]^2 d\ln f_m}, \quad (2.2)$$

where $h_n(f_m)$ is the detector's rms noise at frequency f_m , in a bandwidth equal to frequency, averaged over the sky. Equation (2.2) serves as a definition of $h_{c,m}(f)$. The relation $h_{c,m}(f_m) = h_{o,m}(f_m) \sqrt{2f_m^2/\dot{f}_m}$ then follows from Eq. (29) of Ref. [33] (with the factor of 2 changed to 4 to correct an error), together with the definition of $h_{o,m}$ given above, Eqs. (2.2) and (2.1), and the evaluation of Fourier transforms using the stationary phase approximation.

When the inspiraling object nears the isco, the bandwidth available for building up its signal in the detector becomes less than $\Delta f = f$. A good measure of this reduced bandwidth is $\Delta f = 2(f - f_{\text{isco}})$ (with half of this band below f and half above). This is less than f for $2f_{\text{isco}}/3 < f < f_{\text{isco}}$. Correspondingly, the amplitude of the built-up signal is $\sim h_c \sqrt{2(f_{\text{isco}} - f)/(2f_{\text{isco}}/3)}$. Our modified characteristic amplitude $h'_{c,m} \equiv h_{c,m} \min[1, \sqrt{3(1-f_m/f_{m,\text{isco}})}]$ takes this signal reduction into account.

III. FORMULAS FOR INSPIRAL AND WAVES

In this section we shall give leading-order (in $\tilde{\Omega}^{1/3}$) formulas for the various time-evolving quantities, as functions of the dimensionless orbital angular frequency $\tilde{\Omega}$ and black-hole spin a , and thereby we shall produce exact definitions of the relativistic correction functions. To make clear the magnitudes of various quantities, we shall write some of our formulas numerically in a form relevant to LISA (for which we choose as a fiducial frequency $f_2 = 0.01$ Hz and as a fiducial source, a $\mu = 10M_\odot$ black hole spiraling into a $M = 10^6 M_\odot$ hole at $r_o = 1$ Gpc distance from Earth). We shall also write our formulas in a form relevant to the LIGO-VIRGO network of high-frequency detectors (with, as our fiducial frequency, 100 Hz, and our fiducial source, a $1M_\odot$ neutron star spiraling into a $100M_\odot$ hole at 1 Gpc distance).

In the Newtonian limit, the orbital radius and orbital angular velocity are linked by the Keplerian relation

$$\frac{M}{r} \equiv \frac{1}{\tilde{r}} = (M\Omega)^{2/3} \equiv \tilde{\Omega}^{2/3}. \quad (3.1)$$

This permits us to write the number of orbital radians spent near orbital angular frequency Ω in the following form [cf. Eqs. (3.16) of Misner, Thorne, and Wheeler (MTW) [35], in which a is our orbital radius r]:

TABLE I. $\Omega/\Omega_{\text{isco}}$ (orbital angular velocity in units of that at the isco) as a function of r/r_{isco} (Boyer-Lindquist radius in units of that at the isco) and of a (black-hole angular momentum parameter). For a negative, the hole is counter-rotating relative to the star's orbit; for a positive it is co-rotating. This table was computed from Eqs. (3.18), (3.21) and (3.20). Near the isco, $\Omega/\Omega_{\text{isco}}$ is linear in r/r_{isco} .

r/r_{isco}	-0.99	-0.9	-0.5	0.0	0.2	0.5	0.8	0.9	0.99	0.999
1.000	1.0	1.0	1.0	1.0	1.0	1.0	1.0	1.0	1.0	1.0
1.001	0.9984	0.9984	0.9985	0.9985	0.9985	0.9986	0.9987	0.9988	0.9990	0.9992
1.002	0.9969	0.9969	0.9969	0.9970	0.9971	0.9972	0.9974	0.9976	0.9981	0.9983
1.005	0.9923	0.9923	0.9924	0.9925	0.9927	0.9929	0.9936	0.9940	0.9952	0.9958
1.01	0.9846	0.9847	0.9848	0.9852	0.9854	0.9860	0.9872	0.9882	0.9905	0.9916
1.02	0.9696	0.9697	0.97	0.9707	0.9712	0.9723	0.9747	0.9765	0.9811	0.9833
1.05	0.9269	0.9271	0.9278	0.9294	0.9305	0.9330	0.9386	0.9429	0.9537	0.9590
1.1	0.8624	0.8626	0.8639	0.8668	0.8686	0.8731	0.8831	0.8909	0.9105	0.9204
1.2	0.7538	0.7542	0.7563	0.7607	0.7636	0.7707	0.7869	0.7995	0.8326	0.8497
1.3	0.6664	0.6668	0.6693	0.6747	0.6782	0.6868	0.7066	0.7223	0.7644	0.7866
1.4	0.5947	0.5951	0.5978	0.6037	0.6075	0.6170	0.6389	0.6565	0.7044	0.7303
1.7	0.4419	0.4424	0.4451	0.4512	0.4552	0.4650	0.4884	0.5077	0.5625	0.5937
2.0	0.3450	0.3455	0.3480	0.3536	0.3572	0.3664	0.3885	0.4069	0.4611	0.4930
2.5	0.2460	0.2463	0.2484	0.2530	0.2560	0.2637	0.2823	0.2982	0.3463	0.3758
3.0	0.1867	0.1870	0.1887	0.1925	0.1950	0.2013	0.2168	0.2302	0.2716	0.2976
4.0	0.1210	0.1212	0.1224	0.1250	0.1268	0.1312	0.1423	0.1520	0.1827	0.2025
5.0	0.08643	0.08659	0.08748	0.08944	0.09076	0.09409	0.1024	0.1097	0.1332	0.1487
6.0	0.06570	0.06582	0.06651	0.06804	0.06907	0.07167	0.07817	0.08391	0.1025	0.1149
7.0	0.05211	0.05221	0.05276	0.05399	0.05482	0.05692	0.06217	0.06682	0.08197	0.09211
8.0	0.04264	0.04271	0.04318	0.04419	0.04488	0.04661	0.05097	0.05483	0.06745	0.07595
9.0	0.03572	0.03579	0.03618	0.03704	0.03762	0.03908	0.04276	0.04603	0.05675	0.06399
10.0	0.03049	0.03055	0.03088	0.03162	0.03212	0.03338	0.03654	0.03936	0.04860	0.05486

$$\begin{aligned}
\frac{\Omega^2}{\tilde{\Omega}} &= \frac{d\Phi}{d\ln\Omega} = \frac{5}{96} \frac{1}{\eta} \frac{1}{\tilde{\Omega}^{5/3}} \mathcal{N} \\
&= \frac{1.17 \times 10^5}{(f_2/0.01 \text{ Hz})^{5/3}} \left(\frac{10M_\odot}{\mu} \right) \left(\frac{10^6 M_\odot}{M} \right)^{2/3} \mathcal{N} \\
&= \frac{117}{(f_2/100 \text{ Hz})^{5/3}} \left(\frac{1M_\odot}{\mu} \right) \left(\frac{100M_\odot}{M} \right)^{2/3} \mathcal{N}. \quad (3.2)
\end{aligned}$$

$$\begin{aligned}
N_{\text{orb}} &= \frac{1}{2\pi} \int_{\ln\Omega}^{\ln\Omega_{\text{isco}}} \frac{d\Phi}{d\ln\Omega} d\ln\Omega = \frac{1}{64\pi} \frac{1}{\eta} \frac{1}{\tilde{\Omega}^{5/3}} \mathcal{N}_{\text{orb}} \\
&= \frac{1.11 \times 10^4}{(f_2/0.01 \text{ Hz})^{5/3}} \left(\frac{10M_\odot}{\mu} \right) \left(\frac{10^6 M_\odot}{M} \right)^{2/3} \mathcal{N}_{\text{orb}} \\
&= \frac{11.1}{(f_2/100 \text{ Hz})^{5/3}} \left(\frac{1M_\odot}{\mu} \right) \left(\frac{100M_\odot}{M} \right)^{2/3} \mathcal{N}_{\text{orb}}. \quad (3.4)
\end{aligned}$$

Here \mathcal{N} is the general relativistic correction, which is unity in the ‘‘Newtonian’’ limit $\tilde{\Omega} \ll 1$. Similarly, the total remaining time until the end of the inspiral [Eq. (36.17b) of MTW] is

$$\begin{aligned}
T &= \frac{5}{256} \frac{1}{\eta} \frac{M}{\tilde{\Omega}^{8/3}} \mathcal{T} \\
&= \frac{1.41 \times 10^6 \text{ sec}}{(f_2/0.01 \text{ Hz})^{8/3}} \left(\frac{10M_\odot}{\mu} \right) \left(\frac{10^6 M_\odot}{M} \right)^{2/3} \mathcal{T} \\
&= \frac{0.141 \text{ sec}}{(f_2/100 \text{ Hz})^{8/3}} \left(\frac{1M_\odot}{\mu} \right) \left(\frac{100M_\odot}{M} \right)^{2/3} \mathcal{T}, \quad (3.3)
\end{aligned}$$

and the number of orbits remaining until the end of the inspiral is

By integrating Eq. (3.2) inward to the isco, one can derive the following expression for the general relativistic corrections \mathcal{T} for T and \mathcal{N}_{orb} for N_{orb} in terms of that \mathcal{N} for $\Omega^2/\tilde{\Omega}$:

$$\mathcal{T} = \frac{8}{3} \tilde{\Omega}^{8/3} \int_{\tilde{\Omega}}^{\tilde{\Omega}_{\text{isco}}} \frac{\mathcal{N} d\tilde{\Omega}}{\tilde{\Omega}^{11/3}}, \quad (3.5)$$

$$\mathcal{N}_{\text{orb}} = \frac{5}{3} \tilde{\Omega}^{5/3} \int_{\tilde{\Omega}}^{\tilde{\Omega}_{\text{isco}}} \frac{\mathcal{N} d\tilde{\Omega}}{\tilde{\Omega}^{8/3}}, \quad (3.6)$$

The total energy loss rate [Eq. (3.16) of MTW] is

TABLE II. $\dot{\mathcal{E}}$ (the relativistic correction to $\dot{E}_{\text{GW}} = -\dot{E}$, the total rate of emission of energy into gravitational waves going both to infinity and down the hole), as a function of orbital radius r/r_{isco} and black-hole spin parameter a ; cf. caption of Table I. This table is accurate to four significant digits; each entry was computed by summing over enough spheroidal harmonic orders (l, m) to produce that accuracy.

r/r_{isco}	-0.99	-0.9	-0.5	0.0	0.2	0.5	0.8	0.9	0.99	0.999
1.000	1.240	1.233	1.197	1.143	1.114	1.053	0.9144	0.7895	0.4148	0.2022
1.001	1.239	1.232	1.196	1.142	1.114	1.053	0.9140	0.7894	0.4154	0.2032
1.002	1.238	1.231	1.196	1.141	1.113	1.052	0.9137	0.7894	0.4160	0.2041
1.005	1.235	1.228	1.193	1.139	1.111	1.050	0.9126	0.7891	0.4177	0.2069
1.01	1.231	1.224	1.189	1.135	1.107	1.047	0.9109	0.7887	0.4207	0.2116
1.02	1.222	1.215	1.181	1.127	1.100	1.041	0.9076	0.7880	0.4263	0.2208
1.05	1.198	1.192	1.159	1.108	1.081	1.025	0.8988	0.7867	0.4434	0.2473
1.1	1.165	1.159	1.128	1.080	1.055	1.002	0.8876	0.7859	0.4701	0.2881
1.2	1.115	1.110	1.082	1.039	1.017	0.9706	0.8726	0.7882	0.5182	0.3581
1.3	1.081	1.075	1.051	1.012	0.9913	0.9493	0.8638	0.7920	0.5587	0.4160
1.4	1.055	1.051	1.028	0.9919	0.9733	0.9348	0.8583	0.7960	0.5930	0.4648
1.7	1.011	1.007	0.9888	0.9591	0.9435	0.9119	0.8524	0.8075	0.6665	0.5723
2.0	0.9893	0.9862	0.9705	0.9448	0.9312	0.9034	0.8530	0.8171	0.7117	0.6411
2.5	0.9734	0.9709	0.9580	0.9363	0.9248	0.9012	0.8589	0.8302	0.7556	0.7089
3.0	0.9674	0.9653	0.9542	0.9352	0.9250	0.9040	0.8662	0.8415	0.7813	0.7469
4.0	0.9651	0.9634	0.9546	0.9391	0.9306	0.9129	0.8807	0.8597	0.8121	0.7882
5.0	0.9665	0.9651	0.9577	0.9448	0.9371	0.9216	0.8930	0.8742	0.8320	0.8118
6.0	0.9687	0.9675	0.9611	0.9490	0.9430	0.9291	0.9031	0.8858	0.8469	0.8286
7.0	0.9709	0.9699	0.9641	0.9533	0.9480	0.9354	0.9116	0.8955	0.8589	0.8416
8.0	0.9730	0.9720	0.9669	0.9588	0.9522	0.9407	0.9186	0.9036	0.8689	0.8524
9.0	0.9749	0.9740	0.9693	0.9607	0.9558	0.9452	0.9246	0.9105	0.8774	0.8616
10.0	0.9765	0.9757	0.9714	0.9616	0.9589	0.9491	0.9298	0.9164	0.8847	0.8695

$$\dot{E}_{\text{GW}} = -\dot{E} = \frac{32}{5} \eta^2 \tilde{\Omega}^{10/3} \dot{\mathcal{E}}, \quad (3.7)$$

$$\dot{E}_{\infty 1} = \frac{5}{28} \eta^2 \tilde{\Omega}^4 \mathcal{E}_{\infty 1}, \quad (3.8)$$

where $\dot{\mathcal{E}}$ is the general relativistic correction.

When the object is at large radii (small $\tilde{\Omega}$), the power radiated by the system's mass multipole moments $I^{l, \pm m}$ is of order $\eta^2 \tilde{\Omega}^{2+2l/3}$, while that radiated by its current multipole moments $S^{l, \pm m}$ is of order $\eta^2 \tilde{\Omega}^{2+2(l+1)/3}$ [36]. Correspondingly, the power $\dot{E}_{\infty m}$ radiated to infinity in harmonic m comes almost entirely from the moments of lowest allowed orders l , with the current moments of order l being, *a priori*, comparable to the mass moments of order $l+1$.

For $m=1$, the lowest allowed order for either mass or current is quadrupolar, since gravitational waves are always quadrupolar or higher. For circular orbits in the equatorial plane, the $m=\pm 1$ components of the mass quadrupole moment vanish, so the dominant waves are current quadrupolar $S^{2, \pm 1}$ and mass octupolar $I^{3, \pm 1}$. All other multipolar contributions to $\dot{E}_{\infty 1}$ are smaller than these by at least $(\Omega r)^2 = \tilde{\Omega}^{2/3}$. The contributions of $S^{2, \pm 1}$ to the radiated power $\dot{E}_{\infty 1}$ can be derived from Eqs. (4.16), (5.27), (2.18a,c), (2.7) and (2.8) of Ref. [36], and those of $I^{3, \pm 1}$, from Eqs. (4.16), (5.27), (2.7), and (2.8) of [36]. The sum of these dominant contributions is

where we have tacked on the general relativistic correction factor $\dot{\mathcal{E}}_{\infty 1}$ to account for contributions from all the higher-order multipoles and to make the formula be valid not just for large orbital radii r but for all $r \geq r_{\text{isco}}$. In Eq. (3.8), the numerical factor is $5/28 = 8/45 + 1/1260$, where the big piece $8/45$ is current quadrupolar, while the tiny piece $1/1260$ is mass octupolar.

For harmonic $m \geq 2$, the lowest allowed multipoles are of order $l=m$, and the mass moment $I^{m, \pm m}$ is nonzero so it dominates. All other multipolar contributions to \dot{E}_m are down from these by at least $\tilde{\Omega}^{2/3}$. An expression for \dot{E}_m can be derived from Eqs. (4.16), (5.27), (2.7), and (2.8) of Ref. [36]. The result is

$$\dot{E}_m = \frac{2(m+1)(m+2)(2m+1)! m^{2m+1}}{(m-1)[2^m m! (2m+1)!!]^2} \times \eta^2 \tilde{\Omega}^{2+2m/3} \dot{\mathcal{E}}_{\infty m}, \quad (3.9)$$

where $\dot{\mathcal{E}}_{\infty m}$ is the relativistic correction and $(2m+1)!! \equiv (2m+1)(2m-1)(2m-3) \cdots 1$. For $m=2, 3$, and 4 , this expression reduces to

TABLE III. $\dot{\mathcal{E}}_{\infty 1}$ (the relativistic correction to $\dot{E}_{\infty 1}$, the rate of emission of energy into harmonic-1 gravitational waves with frequency $f_1 = \Omega/2\pi$ traveling to infinity) as a function of orbital radius r/r_{isco} and black-hole spin parameter a ; cf. caption of Table I. This table is accurate to four significant digits; each entry was computed by summing over enough spheroidal harmonic orders $2 \leq l \leq l_{\text{max}}$ at fixed $|m| = 1$ to produce that accuracy.

r/r_{isco}	-0.99	-0.9	-0.5	0.0	0.2	0.5	0.8	0.9	0.99	0.999
1.000	3.013	2.854	2.157	1.320	1.002	0.5530	0.1669	0.06573	0.002762	1.071×10^{-4}
1.001	3.010	2.851	2.156	1.319	1.001	0.5529	0.1670	0.06584	0.002783	1.095×10^{-4}
1.002	3.007	2.849	2.154	1.318	1.001	0.5528	0.1671	0.06595	0.002805	1.119×10^{-4}
1.005	2.998	2.840	2.148	1.316	0.9990	0.5525	0.1675	0.06628	0.002869	1.194×10^{-4}
1.01	2.984	2.827	2.139	1.312	0.9964	0.5520	0.1680	0.06683	0.002979	1.326×10^{-4}
1.02	2.955	2.800	2.121	1.303	0.9915	0.5510	0.1692	0.06793	0.003204	1.619×10^{-4}
1.05	2.876	2.727	2.071	1.280	0.9779	0.5487	0.1729	0.07126	0.003934	2.747×10^{-4}
1.1	2.760	2.619	1.999	1.248	0.9588	0.5462	0.1790	0.07688	0.005322	5.565×10^{-4}
1.2	2.575	2.448	1.885	1.198	0.9305	0.5448	0.1916	0.08821	0.008679	0.001525
1.3	2.434	2.316	1.798	1.161	0.9111	0.5465	0.2040	0.09951	0.01272	0.003073
1.4	2.321	2.213	1.730	1.133	0.8973	0.5498	0.2162	0.1107	0.01733	0.005180
1.7	2.085	1.994	1.588	1.077	0.8719	0.5623	0.2506	0.1421	0.03343	0.01435
2.0	1.940	1.860	1.503	1.049	0.8631	0.5786	0.2799	0.1715	0.05138	0.02648
2.5	1.787	1.719	1.416	1.023	0.8599	0.6045	0.3237	0.2151	0.08223	0.04991
3.0	1.689	1.629	1.361	1.010	0.8621	0.6272	0.3606	0.2527	0.1122	0.07456
4.0	1.567	1.518	1.295	0.9987	0.8704	0.6638	0.4191	0.3143	0.1664	0.1222
5.0	1.493	1.450	1.255	0.9921	0.8789	0.6918	0.4638	0.3627	0.2128	0.1650
6.0	1.441	1.403	1.228	0.9923	0.8865	0.7139	0.4994	0.4020	0.2525	0.2028
7.0	1.403	1.368	1.208	0.9865	0.8930	0.7319	0.5287	0.4346	0.2869	0.2362
8.0	1.373	1.341	1.193	0.9829	0.8987	0.7469	0.5533	0.4624	0.3168	0.2657
9.0	1.349	1.319	1.180	0.9887	0.9035	0.7596	0.5743	0.4863	0.3433	0.2922
10.0	1.329	1.301	1.170	1.005	0.9078	0.7706	0.5925	0.5072	0.3669	0.3159

$$\begin{aligned}\dot{E}_2 &= \frac{32}{5} \eta^2 \tilde{\Omega}^{10/3} \dot{\mathcal{E}}_{\infty 2}, \\ \dot{E}_3 &= \frac{243}{28} \eta^2 \tilde{\Omega}^4 \dot{\mathcal{E}}_{\infty 3}, \\ \dot{E}_4 &= \frac{8192}{567} \eta^2 \tilde{\Omega}^{14/3} \dot{\mathcal{E}}_{\infty 4}.\end{aligned}\quad (3.10)$$

Note that the low- $\tilde{\Omega}$ limit of \dot{E}_2 is identical to that of the total energy loss \dot{E}_{GW} [Eq. (3.7)], as it must be since the $m = 2$ harmonic dominates at low orbital velocities.

From Eqs. (3.8) and (3.9) for \dot{E}_m and the general relationship (2.1) between the waves' amplitude and energy, we obtain the following Newtonian-order expression for the amplitude in harmonic m :

$$h_{o,1} = \sqrt{\frac{5}{7}} \frac{\eta M}{r_o} \tilde{\Omega} \mathcal{H}_{o,1}, \quad (3.11a)$$

$$\begin{aligned}h_{o,m} &= \sqrt{\frac{8(m+1)(m+2)(2m+1)!m^{2m-1}}{(m-1)[2^m m!(2m+1)!!]^2}} \\ &\times \frac{\eta M}{r_o} \tilde{\Omega}^{m/3} \mathcal{H}_{o,m} \quad \text{for } m \geq 2,\end{aligned}\quad (3.11b)$$

where the relativistic correction is related to that for the energy by

$$\mathcal{H}_{o,m} = \sqrt{\dot{\mathcal{E}}_{\infty m}}. \quad (3.12)$$

For the dominant, $m = 2$, radiation Eq. (3.11b) becomes

$$\begin{aligned}h_{o,2} &= \sqrt{\frac{32}{5}} \frac{\eta M}{r_o} \tilde{\Omega}^{2/3} \mathcal{H}_{o,2} \\ &= \frac{3.6 \times 10^{-22}}{r_o/1 \text{ Gpc}} \left(\frac{\mu}{10 M_\odot} \right) \left(\frac{M}{10^6 M_\odot} \right)^{2/3} \left(\frac{f_2}{.01 \text{ Hz}} \right)^{2/3} \mathcal{H}_{o,2} \\ &= \frac{3.6 \times 10^{-23}}{r_o/1 \text{ Gpc}} \left(\frac{\mu}{M_\odot} \right) \left(\frac{M}{100 M_\odot} \right)^{2/3} \left(\frac{f_2}{100 \text{ Hz}} \right)^{2/3} \mathcal{H}_{o,2}.\end{aligned}\quad (3.13)$$

From Eqs. (3.11) for $h_{o,m}$, the definition of $h_{c,m}$ in terms of $h_{o,m}$, the relation $f_m = (m/2\pi)\Omega$, and Eq. (3.2), we obtain the following expression for the characteristic amplitude in harmonic m :

$$h_{c,1} = \frac{5}{\sqrt{672\pi}} \frac{\eta^{1/2} M}{r_o} \tilde{\Omega}^{1/6} \mathcal{H}_{c,1}, \quad (3.14a)$$

TABLE IV. $\dot{\mathcal{E}}_{\infty 2}$ (the relativistic correction to $\dot{E}_{\infty 2}$, the rate of emission of energy into harmonic-2 gravitational waves with frequency $f_2 = 2\Omega/2\pi$ traveling to infinity) as a function of orbital radius r/r_{isco} and black-hole spin parameter a ; cf. caption of Table I. This table is accurate to four significant digits; each entry was computed by summing over enough spheroidal harmonic orders $2 \leq l \leq l_{\text{max}}$ at fixed $|m|=2$ to produce that accuracy.

r/r_{isco}	-0.99	-0.9	-0.5	0.0	0.2	0.5	0.8	0.9	0.99	0.999
1.000	1.029	1.020	0.9734	0.8957	0.8535	0.7653	0.5914	0.4617	0.1656	0.06128
1.001	1.028	1.019	0.9730	0.8954	0.8533	0.7652	0.5915	0.4620	0.1661	0.06170
1.002	1.028	1.019	0.9726	0.8950	0.8530	0.7650	0.5916	0.4624	0.1666	0.06212
1.005	1.026	1.017	0.9713	0.8940	0.8522	0.7645	0.5919	0.4633	0.1681	0.06338
1.01	1.024	1.015	0.9693	0.8925	0.8508	0.7638	0.5925	0.4649	0.1707	0.0655
1.02	1.019	1.011	0.9654	0.8894	0.8483	0.7623	0.5937	0.4680	0.1758	0.06975
1.05	1.007	0.9985	0.9548	0.8813	0.8415	0.7587	0.5974	0.4773	0.1909	0.08241
1.1	0.9900	0.9818	0.9403	0.8704	0.8327	0.7545	0.6037	0.4918	0.2154	0.1038
1.2	0.9648	0.9574	0.9196	0.8558	0.8214	0.7506	0.6165	0.5178	0.2618	0.1465
1.3	0.9480	0.9411	0.9063	0.8474	0.8156	0.7504	0.6287	0.5402	0.3039	0.1881
1.4	0.9364	0.9301	0.8977	0.8427	0.8131	0.7523	0.6400	0.5597	0.3417	0.2277
1.7	0.9191	0.9138	0.8867	0.8403	0.8151	0.7635	0.6697	0.6050	0.4309	0.3303
2.0	0.9138	0.9092	0.8857	0.8450	0.8227	0.7769	0.6941	0.6382	0.4930	0.4077
2.5	0.9144	0.9106	0.8910	0.8566	0.8377	0.7983	0.7268	0.6791	0.5617	0.4954
3.0	0.9187	0.9154	0.8984	0.8684	0.8517	0.8167	0.7525	0.7097	0.6075	0.5524
4.0	0.9286	0.9260	0.9125	0.8882	0.8745	0.8453	0.7908	0.7542	0.6680	0.6241
5.0	0.9372	0.9351	0.9237	0.9034	0.8914	0.8662	0.8183	0.7857	0.7085	0.6699
6.0	0.9442	0.9424	0.9326	0.9142	0.9043	0.8821	0.8391	0.8095	0.7387	0.7033
7.0	0.9499	0.9483	0.9396	0.9232	0.9145	0.8945	0.8554	0.8282	0.7625	0.7295
8.0	0.9545	0.9531	0.9453	0.9323	0.9226	0.9044	0.8686	0.8434	0.7819	0.7507
9.0	0.9584	0.9571	0.9500	0.9369	0.9293	0.9126	0.8795	0.8560	0.7981	0.7685
10.0	0.9616	0.9604	0.9540	0.9400	0.9349	0.9195	0.8887	0.8666	0.8119	0.7837

$$h_{c,m} = \sqrt{\frac{5(m+1)(m+2)(2m+1)!m^{2m}}{12\pi(m-1)[2^m m!(2m+1)!!]^2}} \times \frac{\eta^{1/2} M}{r_o} \tilde{\Omega}^{(2m-5)/6} \mathcal{H}_{c,m} \quad \text{for } m \geq 2, \quad (3.14b)$$

where [using Eq. (3.12)] the relativistic correction is related to earlier ones by

$$\mathcal{H}_{c,m} = \sqrt{\mathcal{N} \dot{\mathcal{E}}_{\infty m}}. \quad (3.15)$$

For $m=2$, expression (3.14b) becomes

$$\begin{aligned} h_{c,2} &= \sqrt{\frac{2}{3}} \frac{\eta^{1/2} M}{\pi r_o \tilde{\Omega}^{1/6}} \mathcal{H}_{c,2} \\ &= \frac{1.0 \times 10^{-19}}{r_o/1 \text{ Gpc}} \left(\frac{\mu}{10M_\odot} \right)^{1/2} \left(\frac{M}{10^6 M_\odot} \right)^{1/3} \left(\frac{.01 \text{ Hz}}{f_2} \right)^{1/6} \mathcal{H}_{c,2} \\ &= \frac{3.2 \times 10^{-22}}{r_o/1 \text{ Gpc}} \left(\frac{\mu}{M_\odot} \right)^{1/2} \left(\frac{M}{100M_\odot} \right)^{1/3} \left(\frac{100 \text{ Hz}}{f_2} \right)^{1/6} \mathcal{H}_{c,2}. \end{aligned} \quad (3.16)$$

All of the relativistic correction functions can be expressed analytically in terms of $\dot{\mathcal{E}}$, and $\dot{\mathcal{E}}_{\infty m}$. This has almost been done already: The correction functions \mathcal{I} , $\mathcal{H}_{o,m}$ and

$\mathcal{H}_{c,m}$ have been expressed in terms of $\dot{\mathcal{E}}$, $\dot{\mathcal{E}}_{\infty m}$, \mathcal{N} and $\tilde{\Omega}_{\text{isco}}$ by Eqs. (3.5), (3.12) and (3.15) respectively. All that remains is to derive an expression for \mathcal{N} in terms of $\dot{\mathcal{E}}$, and an expression for $\tilde{\Omega}_{\text{isco}}$.

The derivations are based on the Kerr-metric relations

$$E = -\eta M \frac{1 - 2/\tilde{r} + a/\tilde{r}^{3/2}}{\sqrt{1 - 3/\tilde{r} + 2a/\tilde{r}^{3/2}}} \quad (3.17)$$

for the object's total energy in terms of its dimensionless orbital radius \tilde{r} [Eq. (5.4.7b) of Ref. [37]] and

$$\tilde{r} = (\tilde{\Omega}^{-1} - a)^{2/3} \quad (3.18)$$

for its orbital radius in terms of its orbital angular velocity [Eq. (2.16) of Ref. [32]]. By differentiating these equations with respect to time and combining with each other and with Eqs. (3.2) and (3.7) for $\Omega^2/\tilde{\Omega}$ and $\dot{E}_{\text{GW}} = -\dot{E}$, we obtain

$$\begin{aligned} \mathcal{N} &= \frac{1}{\dot{\mathcal{E}}} \left(1 + \frac{a}{\tilde{r}^{3/2}} \right)^{5/3} \left(1 - \frac{6}{\tilde{r}} + \frac{8a}{\tilde{r}^{3/2}} - \frac{3a^2}{\tilde{r}^2} \right) \\ &\quad \times \left(1 - \frac{3}{\tilde{r}} + \frac{2a}{\tilde{r}^{3/2}} \right)^{-3/2}. \end{aligned} \quad (3.19)$$

TABLE V. $\hat{\mathcal{E}}_{\infty 3}$ (the relativistic correction to $\dot{E}_{\infty 3}$, the rate of emission of energy into harmonic-3 gravitational waves with frequency $f_3 = 3\Omega/2\pi$ traveling to infinity) as a function of orbital radius r/r_{isco} and black-hole spin parameter a ; cf. caption of Table I. This table is accurate to four significant digits; each entry was computed by summing over enough spheroidal harmonic orders $2 \leq l \leq l_{\text{max}}$ at fixed $|m| = 3$ to produce that accuracy.

r/r_{isco}	-0.99	-0.9	-0.5	0.0	0.2	0.5	0.8	0.9	0.99	0.999
1.000	0.9753	0.9614	0.8926	0.7848	0.7309	0.6292	0.4684	0.3712	0.1573	0.06456
1.001	0.9748	0.9608	0.8922	0.7845	0.7307	0.6291	0.4685	0.3714	0.1577	0.06495
1.002	0.9742	0.9603	0.8917	0.7842	0.7304	0.6289	0.4685	0.3715	0.1581	0.06534
1.005	0.9726	0.9587	0.8904	0.7832	0.7296	0.6285	0.4685	0.3719	0.1592	0.06651
1.01	0.9699	0.9561	0.8882	0.7817	0.7284	0.6277	0.4686	0.3725	0.1610	0.06846
1.02	0.9648	0.9512	0.8841	0.7787	0.7260	0.6263	0.4688	0.3739	0.1646	0.07237
1.05	0.9507	0.9376	0.8729	0.7708	0.7197	0.6229	0.4699	0.3780	0.1751	0.08391
1.1	0.9313	0.9189	0.8576	0.7606	0.7118	0.6191	0.4728	0.3852	0.1919	0.1026
1.2	0.9033	0.8921	0.8365	0.7476	0.7026	0.6166	0.4806	0.3998	0.2223	0.1374
1.3	0.8849	0.8747	0.8235	0.7411	0.6990	0.6183	0.4900	0.4141	0.2489	0.1686
1.4	0.8728	0.8633	0.8157	0.7385	0.6988	0.6223	0.5000	0.4278	0.2722	0.1963
1.7	0.8562	0.8483	0.8085	0.7424	0.7078	0.6402	0.5301	0.4649	0.3280	0.2627
2.0	0.8534	0.8466	0.8117	0.7531	0.7221	0.6603	0.5580	0.4969	0.3701	0.3114
2.5	0.8588	0.8531	0.8239	0.7737	0.7466	0.6919	0.5986	0.5417	0.4238	0.3710
3.0	0.8676	0.8627	0.8373	0.7929	0.7687	0.7190	0.6324	0.5785	0.4657	0.4156
4.0	0.8851	0.8811	0.8606	0.8243	0.8040	0.7616	0.6850	0.6358	0.5297	0.4822
5.0	0.8993	0.8961	0.8788	0.8477	0.8301	0.7929	0.7240	0.6786	0.5780	0.5320
6.0	0.9106	0.9078	0.8928	0.8658	0.8500	0.8168	0.7541	0.7119	0.6164	0.5717
7.0	0.9198	0.9172	0.9039	0.8787	0.8657	0.8356	0.7780	0.7387	0.6478	0.6045
8.0	0.9272	0.9249	0.9130	0.8902	0.8783	0.8508	0.7975	0.7607	0.6741	0.6322
9.0	0.9334	0.9313	0.9204	0.9004	0.8887	0.8633	0.8137	0.7791	0.6965	0.6559
10.0	0.9386	0.9367	0.9267	0.9087	0.8974	0.8739	0.8275	0.7948	0.7158	0.6766

When \tilde{r} is regarded as the function (3.18) of $\tilde{\Omega}$, this becomes the desired expression for \mathcal{N} in terms of $\hat{\mathcal{E}}$ and $\tilde{\Omega}$.

The innermost stable circular orbit (isco) is at the location \tilde{r}_{isco} where the object's total energy $E(\tilde{r})$ is a minimum or, equivalently, where $\tilde{\Omega}$ is infinite or, equivalently, where \mathcal{N} vanishes; i.e., \tilde{r}_{isco} is that root of the quartic equation $\tilde{r}^2 - 6\tilde{r} + 8a\tilde{r}^{1/2} - 3a^2 = 0$ which lies between 1 (when $a = 1$) and 6 (when $a = 0$). An analytic expression for r_{isco} has been given by Bardeen, Press, and Teukolsky [32]:

$$\begin{aligned} \tilde{r}_{\text{isco}} &= 3 + Z_2 - \text{sgn}(a)[(3 - Z_1)(3 + Z_1 + 2Z_2)]^{1/2}, \\ Z_1 &\equiv 1 + (1 - a^2)^{1/3}[(1 + a)^{1/3} + (1 - a)^{1/3}], \\ Z_2 &\equiv (3a^2 + Z_1^2)^{1/2}. \end{aligned} \quad (3.20)$$

The dimensionless orbital angular velocity at the isco $\tilde{\Omega}_{\text{isco}}$ is expressed in terms of this \tilde{r}_{isco} by Eq. (3.18):

$$\tilde{\Omega}_{\text{isco}} = \frac{1}{\tilde{r}_{\text{isco}}^{3/2 + a}}. \quad (3.21)$$

We note, in passing, approximate analytic formulas for the relativistic corrections \mathcal{T} and \mathcal{N}_{orb} to the time T and number of remaining orbits \mathcal{N}_{orb} until the end of inspiral—for the

special case of a nonspinning black hole, $a = 0$. Inserting expression (3.19) into Eqs. (3.5) and (3.6), and noting from Table II that in each of these equations $\hat{\mathcal{E}}$ is a much more slowly varying function of the integration variable than the rest of the integrand, we pull $\hat{\mathcal{E}}$ out of the integral (i.e., we perform the first step of an integration by parts) and then perform the integration analytically. The results are

$$\begin{aligned} \mathcal{T} \approx \frac{1}{\hat{\mathcal{E}}} &\left[\frac{1 - \frac{7}{2}u - \frac{147}{8}u^2 - \frac{2205}{16}u^3 + \frac{19845}{16}u^4}{\sqrt{1 - 3u}} \right. \\ &\left. - \frac{4671}{8\sqrt{2}}u^4 + \frac{19845}{32}u^4 \ln\left(\frac{3(1 + \sqrt{2})^2 u}{(1 + \sqrt{1 - 3u})^2}\right) \right], \end{aligned} \quad (3.22)$$

$$\mathcal{N}_{\text{orb}} \approx \frac{1}{\hat{\mathcal{E}}} \left(\frac{1 - 4u - 48u^2 + 288u^3}{\sqrt{1 - 3u}} - 24\sqrt{3}u^5 \right), \quad (3.23)$$

where $u = \tilde{\Omega}^{2/3} = 1/\tilde{r}$. These formulas agree with the numeri-

TABLE VI. $\hat{\mathcal{E}}_{\infty 4}$ (the relativistic correction to $\dot{E}_{\infty 4}$, the rate of emission of energy into harmonic-4 gravitational waves with frequency $f_4 = 4\Omega/2\pi$ traveling to infinity) as a function of orbital radius r/r_{isco} and black-hole spin parameter a ; cf. caption of Table I. This table is accurate to four significant digits; each entry was computed by summing over enough spheroidal harmonic orders $2 \leq l \leq l_{\text{max}}$ at fixed $|m| = 4$ to produce that accuracy.

r/r_{isco}	-0.99	-0.9	-0.5	0.0	0.2	0.5	0.8	0.9	0.99	0.999
1.000	0.9393	0.9209	0.8319	0.6981	0.6342	0.5196	0.3574	0.2720	0.1116	0.04673
1.001	0.9387	0.9203	0.8314	0.6978	0.6339	0.5194	0.3574	0.2721	0.1118	0.04699
1.002	0.9380	0.9197	0.8309	0.6975	0.6337	0.5193	0.3575	0.2722	0.1120	0.04726
1.005	0.9361	0.9179	0.8295	0.6965	0.6329	0.5189	0.3575	0.2725	0.1127	0.04807
1.01	0.9330	0.9149	0.8271	0.6949	0.6317	0.5183	0.3576	0.2730	0.1139	0.04940
1.02	0.9270	0.9091	0.8225	0.6920	0.6295	0.5171	0.3578	0.2739	0.1163	0.05207
1.05	0.9106	0.8935	0.8102	0.6841	0.6235	0.5143	0.3589	0.2770	0.1231	0.05993
1.1	0.8881	0.8720	0.7936	0.6740	0.6162	0.5115	0.3617	0.2826	0.1342	0.07255
1.2	0.8560	0.8416	0.7709	0.6618	0.6084	0.5109	0.3697	0.2947	0.1547	0.09588
1.3	0.8353	0.8221	0.7573	0.6563	0.6064	0.5143	0.3793	0.3073	0.1731	0.1168
1.4	0.8218	0.8097	0.7496	0.6549	0.6077	0.5199	0.3897	0.3198	0.1898	0.1355
1.7	0.8035	0.7943	0.7440	0.6627	0.6212	0.5424	0.4217	0.3555	0.2325	0.1821
2.0	0.8021	0.7934	0.7493	0.6774	0.6398	0.5669	0.4523	0.3880	0.2676	0.2190
2.5	0.8109	0.8036	0.7664	0.7037	0.6710	0.6052	0.4977	0.4355	0.3163	0.2683
3.0	0.8232	0.8169	0.7843	0.7286	0.6984	0.6383	0.5365	0.4759	0.3570	0.3086
4.0	0.8466	0.8416	0.8151	0.7687	0.7432	0.6905	0.5983	0.5409	0.4233	0.3737
5.0	0.8656	0.8614	0.8389	0.7987	0.7765	0.7297	0.6450	0.5910	0.4758	0.4257
6.0	0.8807	0.8770	0.8574	0.8227	0.8021	0.7599	0.6818	0.6306	0.5190	0.4689
7.0	0.8928	0.8895	0.8720	0.8412	0.8224	0.7838	0.7115	0.6631	0.5551	0.5055
8.0	0.9026	0.8997	0.8839	0.8546	0.8388	0.8033	0.7359	0.6902	0.5859	0.5371
9.0	0.9108	0.9081	0.8938	0.8673	0.8523	0.8195	0.7563	0.7130	0.6125	0.5647
10.0	0.9177	0.9152	0.9020	0.8759	0.8637	0.8331	0.7737	0.7326	0.6355	0.5889

cal values of \mathcal{T} and \mathcal{N}_{orb} in Tables IX and X below to within 3% at $6.02 < \tilde{r} < 18$ and to within 1% at $6 \leq \tilde{r} < 6.02$ and $\tilde{r} > 18$.

IV. TABLES OF RELATIVISTIC CORRECTION FUNCTIONS

We shall use two dimensionless parameters to measure the distance of an orbit from the isco: the ratio $r/r_{\text{isco}} \equiv \tilde{r}/\tilde{r}_{\text{isco}}$ of the orbit's Boyer-Lindquist radial coordinate r to its value at the isco and the ratio $\Omega/\Omega_{\text{isco}} \equiv \tilde{\Omega}/\tilde{\Omega}_{\text{isco}}$ of the orbit's angular velocity to that at the isco. The relationship between these two parameters is given by Eqs. (3.18), (3.20) and (3.21), and is tabulated in Table I.

We have integrated the Teukolsky-Sasaki-Nakamura equation for perturbations of a Kerr black hole, to obtain the functions $\hat{\mathcal{E}}(\tilde{\Omega})$, and $\hat{\mathcal{E}}_{\infty m}(\tilde{\Omega})$ and we have then used Eqs. (3.18), (3.19), (3.5) and (3.6) to compute \mathcal{N} , \mathcal{T} and \mathcal{N}_{orb} . These functions are listed in Tables II–X and some of our numerical methods are described in the Appendix. As a by-product of these calculations, we have inferred what fraction $\dot{E}/\dot{E}_{\text{GW}}$ of the total rate of energy emission goes down the hole's horizon; that fraction is shown in Table VII.

V. APPLICATIONS TO LISA

A. LISA noise

Tentative error budgets for LISA are spelled out in Tables 4.1 and 4.2 of the LISA Pre-Phase-A Report [38]. Various

researchers have computed LISA noise spectra from those error budgets. It is conventional, for LISA, to characterize the noise by the sensitivity to periodic sources for 1 yr integration time and a signal-to-noise ratio of 5, averaged over source directions and polarizations (“sky averaged”). We shall denote this quantity by $h_{\text{SN5,1 yr}}^{\text{SA}}$. It is related to the sky-averaged spectral density introduced in the paragraph before Eq. (2.1) by $h_{\text{SN5,1 yr}}^{\text{SA}} = 5\sqrt{S_h^{\text{SA}}\Delta f}$, where $\Delta f = 1/1 \text{ yr}$ is the bandwidth for the one-year integration time; and correspondingly, it is related to the sky-averaged rms noise in a bandwidth equal to frequency, $h_n(f) = \sqrt{fS_h^{\text{SA}}(f)}$ (which we use in this paper), by

$$h_n(f) = \frac{1}{5} \sqrt{\frac{f}{\Delta f}} h_{\text{SN5,1 yr}}^{\text{SA}}(f). \quad (5.1)$$

We have deduced $h_n(f)$ using this equation and the values of $h_{\text{SN5,1 yr}}^{\text{SA}}(f)$ computed by various researchers [39–41]; we plot it as a thick solid curve in Figs. 3–7 below.

It is likely that LISA's performance will be compromised at $f \leq 0.003 \text{ Hz}$ by a stochastic background due to white-dwarf binaries. The most recent estimate of that stochastic background is by Hils and Bender [42]; it agrees satisfactorily with an estimate by Webbink and Han [43]. We have used a simple piecewise straight-line fit to the logarithm of the Hils-Bender white-dwarf-background noise curve:

TABLE VII. $\dot{E}_H/\dot{E}_{\text{GW}}$ (the ratio of the energy radiated down the hole to the total energy radiated) as a function of orbital radius r/r_{isco} and black-hole spin parameter a ; cf. caption of Table I. This table is accurate to three significant digits; each entry was computed by summing over enough spheroidal harmonic orders (l, m) to produce that accuracy.

r/r_{ms}	-0.99	-0.9	-0.5	0.0	0.2	0.5	0.8	0.9	0.99	0.999
1.000	0.0129	0.0118	0.00757	0.00319	0.00162	-0.00222	-0.0166	-0.0341	-0.0942	-0.129
1.001	0.0129	0.0118	0.00753	0.00318	0.00161	-0.00222	-0.0165	-0.0341	-0.0942	-0.129
1.002	0.0128	0.0117	0.00750	0.00316	0.00160	-0.00222	-0.0165	-0.0341	-0.0942	-0.129
1.005	0.0127	0.0116	0.00740	0.00310	0.00156	-0.00224	-0.0165	-0.0340	-0.0941	-0.129
1.01	0.0124	0.0114	0.00723	0.00301	0.00149	-0.00225	-0.0164	-0.0339	-0.0941	-0.129
1.02	0.0120	0.0109	0.00691	0.00284	0.00137	-0.00228	-0.0163	-0.0337	-0.0939	-0.129
1.05	0.0107	0.00975	0.00606	0.00239	0.00106	-0.00233	-0.0159	-0.0330	-0.0930	-0.128
1.1	0.00898	0.00814	0.00493	0.00182	6.92×10^{-4}	-0.00234	-0.0151	-0.0316	-0.0906	-0.125
1.2	0.00651	0.00586	0.00339	0.00111	2.72×10^{-4}	-0.00219	-0.0137	-0.0285	-0.0834	-0.116
1.3	0.00489	0.00438	0.00244	7.21×10^{-4}	7.09×10^{-5}	-0.00198	-0.0122	-0.0254	-0.0764	-0.107
1.4	0.00378	0.00336	0.00182	4.89×10^{-4}	-2.80×10^{-5}	-0.00177	-0.0109	-0.0227	-0.0692	-0.0980
1.7	0.00198	0.00174	8.80×10^{-4}	1.85×10^{-4}	-1.08×10^{-4}	-0.00125	-0.00781	-0.0164	-0.0519	-0.0754
2.0	0.00118	0.00103	5.00×10^{-4}	8.52×10^{-5}	-1.01×10^{-4}	-9.03×10^{-4}	-0.00570	-0.0123	-0.0396	-0.0586
2.5	6.03×10^{-4}	5.22×10^{-4}	2.41×10^{-4}	3.07×10^{-5}	-7.20×10^{-5}	-5.60×10^{-4}	-0.00359	-0.00792	-0.0264	-0.0401
3.0	3.55×10^{-4}	3.05×10^{-4}	1.37×10^{-4}	1.37×10^{-5}	-5.01×10^{-5}	-3.71×10^{-4}	-0.00241	-0.00539	-0.0186	-0.0287
4.0	1.58×10^{-4}	1.35×10^{-4}	5.88×10^{-5}	3.94×10^{-6}	-2.64×10^{-5}	-1.89×10^{-4}	-0.00125	-0.00284	-0.0103	-0.0164
5.0	8.62×10^{-5}	7.34×10^{-5}	3.13×10^{-5}	1.53×10^{-6}	-1.55×10^{-5}	-1.10×10^{-4}	-7.41×10^{-4}	-0.00169	-0.00637	-0.0103
6.0	5.29×10^{-5}	4.50×10^{-5}	1.90×10^{-5}	7.13×10^{-7}	-9.97×10^{-6}	-7.02×10^{-5}	-4.77×10^{-4}	-0.00101	-0.00424	-0.00693
7.0	3.52×10^{-5}	2.99×10^{-5}	1.25×10^{-5}	3.75×10^{-7}	-6.82×10^{-6}	-4.79×10^{-5}	-3.27×10^{-4}	-7.56×10^{-4}	-0.00297	-0.00491
8.0	2.48×10^{-5}	2.10×10^{-5}	8.74×10^{-6}	2.16×10^{-7}	-4.89×10^{-6}	-3.43×10^{-5}	-2.35×10^{-4}	-5.46×10^{-4}	-0.00217	-0.00362
9.0	1.82×10^{-5}	1.54×10^{-5}	6.40×10^{-6}	1.33×10^{-7}	-3.65×10^{-6}	-2.55×10^{-5}	-1.76×10^{-4}	-4.09×10^{-4}	-0.00164	-0.00275
10.0	1.39×10^{-5}	1.17×10^{-5}	4.85×10^{-6}	8.63×10^{-8}	-2.80×10^{-6}	-1.96×10^{-5}	-1.35×10^{-4}	-3.15×10^{-4}	-0.00127	-0.00214

TABLE VIII. \mathcal{N} (the relativistic correction to $\Omega^2/\dot{\Omega} = d\Phi/d\ln\Omega$, the number of radians of orbital inspiral per unit fractional change of orbital angular velocity), as a function of orbital radius r/r_{isco} and black-hole spin parameter a ; cf. caption of Table I. This table is accurate to four significant digits, and it was computed using Eq. (3.19) and \mathcal{E} from Table II. Near the isco, $\mathcal{N} \propto \tilde{r} - \tilde{r}_{\text{isco}} \propto \tilde{\Omega} - \tilde{\Omega}_{\text{isco}}$.

r/r_{isco}	-0.99	-0.9	-0.5	0.0	0.2	0.5	0.8	0.9	0.99	0.999
1.000	0.0	0.0	0.	0.0	0.0	0.0	0.0	0.0	0.0	0.0
1.001	0.001966	0.001995	0.002150	0.002471	0.002685	0.003262	0.005188	0.007911	0.03914	0.1960
1.002	0.003927	0.003984	0.004294	0.004932	0.005360	0.006510	0.01034	0.01575	0.07756	0.3844
1.005	0.009777	0.009917	0.01068	0.01227	0.01332	0.01616	0.02560	0.03888	0.1886	0.9077
1.01	0.01942	0.01969	0.02120	0.02432	0.02639	0.03195	0.05037	0.07612	0.3605	1.656
1.02	0.03831	0.03883	0.04176	0.04778	0.05177	0.06246	0.09754	0.1460	0.6605	2.785
1.05	0.09192	0.09314	0.09979	0.1134	0.1224	0.1462	0.2224	0.3244	1.296	4.447
1.1	0.1721	0.1742	0.1857	0.2090	0.2242	0.2639	0.3865	0.5431	1.836	4.964
1.2	0.3043	0.3076	0.3251	0.3599	0.3824	0.4397	0.6066	0.8039	2.133	4.385
1.3	0.4078	0.4116	0.4321	0.4725	0.4983	0.5628	0.7424	0.9427	2.115	3.725
1.4	0.4901	0.4941	0.5160	0.5589	0.5857	0.6524	0.8315	1.022	2.026	3.228
1.7	0.6564	0.6603	0.6820	0.7239	0.7498	0.8119	0.9671	1.117	1.761	2.373
2.0	0.7537	0.7574	0.7771	0.8147	0.8378	0.8923	1.022	1.140	1.589	1.965
2.5	0.8452	0.8482	0.8644	0.8955	0.9142	0.9579	1.057	1.142	1.427	1.637
3.0	0.8949	0.8975	0.9110	0.9370	0.9526	0.9886	1.068	1.134	1.338	1.477
4.0	0.9445	0.9463	0.9564	0.9757	0.9873	1.014	1.071	1.116	1.245	1.324
5.0	0.9673	0.9688	0.9768	0.9917	1.001	1.022	1.067	1.101	1.195	1.250
6.0	0.9797	0.9809	0.9874	1.001	1.008	1.025	1.061	1.089	1.164	1.207
7.0	0.9870	0.9880	0.9936	1.005	1.011	1.025	1.056	1.080	1.143	1.177
8.0	0.9916	0.9925	0.9973	1.005	1.012	1.025	1.052	1.072	1.126	1.156
9.0	0.9947	0.9954	0.9998	1.008	1.013	1.024	1.048	1.066	1.114	1.140
10.0	0.9968	0.9975	1.001	1.011	1.013	1.023	1.045	1.061	1.104	1.127

TABLE IX. \mathcal{T} (the relativistic correction to T , the time remaining until the isco is reached) as a function of the orbital radius r/r_{isco} and black-hole spin parameter a ; cf. caption of Table I. Near the isco, $\mathcal{T} \approx (8/5) \mathcal{N}_{\text{orb}} \propto (\tilde{r} - \tilde{r}_{\text{isco}})^2 \propto (\tilde{\Omega} - \tilde{\Omega}_{\text{isco}})^2$. We think this table is accurate to about 1 part in 500, except at $r/r_{\text{isco}} \lesssim 1.2$ where the accuracy is about 1 part in 100. The table was computed from Eqs. (3.18), (3.19), and (3.5), using a cubic interpolation to $\tilde{\mathcal{E}}(r/r_{\text{isco}})$ as given in Table II.

r/r_{isco}	-0.99	-0.9	-0.5	0.0	0.2	0.5	0.8	0.9	0.99	0.999
1.000	0.0	0.0	0.0	0.0	0.0	0.0	0.0	0.0	0.0	0.0
1.001	4.08×10^{-6}	4.13×10^{-6}	4.40×10^{-6}	4.93×10^{-6}	5.28×10^{-6}	6.16×10^{-6}	8.93×10^{-6}	1.26×10^{-5}	5.01×10^{-5}	2.22×10^{-4}
1.002	1.63×10^{-5}	1.65×10^{-5}	1.75×10^{-5}	1.97×10^{-5}	2.10×10^{-5}	2.46×10^{-5}	3.56×10^{-5}	5.02×10^{-5}	1.99×10^{-4}	8.75×10^{-4}
1.005	1.01×10^{-4}	1.02×10^{-4}	1.09×10^{-4}	1.22×10^{-4}	1.30×10^{-4}	1.52×10^{-4}	2.20×10^{-4}	3.10×10^{-4}	0.00122	0.00525
1.01	3.97×10^{-4}	4.02×10^{-4}	4.28×10^{-4}	4.80×10^{-4}	5.13×10^{-4}	5.98×10^{-4}	8.62×10^{-4}	0.00121	0.00470	0.0196
1.02	0.00154	0.00156	0.00166	0.00186	0.00199	0.00231	0.00332	0.00464	0.0175	0.0692
1.05	0.00883	0.00893	0.00949	0.0106	0.0113	0.0131	0.0186	0.0256	0.0897	0.309
1.1	0.0307	0.0311	0.0329	0.0366	0.0389	0.0448	0.0623	0.0842	0.266	0.778
1.2	0.0950	0.0960	0.101	0.112	0.118	0.134	0.181	0.237	0.642	1.53
1.3	0.169	0.171	0.180	0.196	0.207	0.233	0.306	0.390	0.947	2.00
1.4	0.243	0.245	0.257	0.279	0.293	0.327	0.420	0.524	1.17	2.26
1.7	0.432	0.435	0.452	0.484	0.503	0.550	0.674	0.802	1.49	2.45
2.0	0.568	0.571	0.589	0.624	0.645	0.696	0.823	0.949	1.56	2.33
2.5	0.712	0.715	0.732	0.766	0.786	0.834	0.950	1.06	1.52	2.04
3.0	0.796	0.799	0.815	0.846	0.864	0.907	1.01	1.10	1.45	1.81
4.0	0.886	0.888	0.901	0.925	0.940	0.974	1.05	1.11	1.34	1.53
5.0	0.929	0.931	0.941	0.961	0.973	1.00	1.06	1.11	1.27	1.39
6.0	0.953	0.954	0.963	0.980	0.990	1.01	1.06	1.10	1.22	1.31
7.0	0.967	0.968	0.976	0.990	0.999	1.02	1.06	1.09	1.19	1.26
8.0	0.976	0.978	0.984	0.997	1.00	1.02	1.06	1.09	1.17	1.22
9.0	0.983	0.984	0.990	1.00	1.01	1.02	1.05	1.08	1.15	1.19
10.0	0.987	0.988	0.993	1.00	1.01	1.02	1.05	1.07	1.14	1.17

straight lines that join the following points in $(\log_{10} f, \log_{10} h_{\text{SN5,1 yr}}^{\text{SA}})$ where f is measured in Hz:

$$(-4, -20.518), \quad (-3.62, -20.737), \quad (-2.78, -21.66), \\ (-2.61, -22.90), \quad (-2, -23.731). \quad (5.2)$$

This white-dwarf noise, converted to our conventions via Eq. (5.1), is shown as a thick dashed curve in Figs. 3–7 below.

B. Detectable systems

Of greatest interest, for probing the spacetime geometries of massive black holes, is the gravitational radiation emitted during the last year of inspiral of a compact object. In planning the LISA mission, it is important to know the detectability of these final-year waves, as a function of the system's parameters: the hole's mass M and spin a , the object's mass μ , and the distance r_o from Earth. Previous studies of this issue [39,38] have assumed that the massive hole is non-spinning, $a=0$.

It is straightforward to compute the rms signal to noise ratio $(S/N)_{\text{rms}}$ (averaged over detector and system orientations) from Eq. (2.2), using the noise amplitudes h_n described above and the dominant $m=2$ characteristic amplitude $h_{c,2}$ of Eqs. (3.16) and (3.15), with \mathcal{N} and $\tilde{\mathcal{E}}_{\infty m}$ taken

from Tables VIII and IV. In this calculation, the frequency $f_2 = \Omega/\pi$ ranges from its value at time $T=1$ y [Eq. (3.3) and Table IX] to its value at the isco.

In view of the complexity of the data analysis for these waves, a signal to noise ratio of about 10 may be required for their detection, and in view of the estimated event rates (Sec. I), it is necessary that LISA see out to at least $r_o=1$ Gpc. Accordingly, we have computed the range of masses μ and M and black-hole spins a for which $(S/N)_{\text{rms}} > 10$ at a distance $r_o=1$ Gpc. This range of ‘‘detectable systems’’ is shown in Fig. 1 for LISA without the white-dwarf background (solid curves) and with the background (dashed curves) [44].

Several features of this figure deserve comment:

(i) Inspiring white dwarfs and neutron stars ($\mu \lesssim 1.4M_{\odot}$) are barely detectable, with $(S/N)_{\text{rms}}=10$, at 1 Gpc. It would be highly desirable to reduce LISA's design noise floor by a factor of 2 or 3, to give greater confidence of detection.

(ii) For $\mu=10M_{\odot}$ inspiraling black holes, the detectable systems have a wide range of central black-hole masses: $10^4 M_{\odot} \lesssim M \lesssim 10^7 M_{\odot}$.

(iii) The upper limit on detectable central-hole masses M depends strongly on the black-hole spin: for $\mu=10M_{\odot}$ it ranges from $2 \times 10^6 M_{\odot}$ to $3 \times 10^7 M_{\odot}$ without the white-dwarf background and from 1×10^6 to 1.5×10^7 with the background. (The spins shown are for no rotation $a=0$, and

TABLE X. \mathcal{N}_{orb} (the relativistic correction to N_{orb} , the number of orbits remaining until the isco is reached) as a function of orbital radius r/r_{isco} and black-hole spin parameter a ; cf. caption of Table I. Near the isco, $\mathcal{T} \approx (8/5)\mathcal{N}_{\text{orb}} \propto (\tilde{r} - \tilde{r}_{\text{isco}})^2 \propto (\tilde{\Omega} - \tilde{\Omega}_{\text{isco}})^2$. We think this table is accurate to about 1 part in 500, except at $r/r_{\text{isco}} \leq 1.2$ where the accuracy is about 1 part in 100. The table was computed from Eqs. (3.18), (3.19), and (3.6), using a cubic interpolation to $\dot{\mathcal{E}}(r/r_{\text{isco}})$ as given in Table II.

r/r_{isco}	-0.99	-0.9	-0.5	0.0	0.2	0.5	0.8	0.9	0.99	0.999
1.000	0.0	0.0	0.0	0.0	0.0	0.0	0.0	0.0	0.0	0.0
1.001	2.55×10^{-6}	2.58×10^{-6}	2.75×10^{-6}	3.09×10^{-6}	3.30×10^{-6}	3.85×10^{-6}	5.58×10^{-6}	7.88×10^{-6}	3.13×10^{-5}	1.39×10^{-4}
1.002	1.02×10^{-5}	1.03×10^{-5}	1.10×10^{-5}	1.23×10^{-5}	1.32×10^{-5}	1.54×10^{-5}	2.23×10^{-5}	3.14×10^{-5}	1.25×10^{-4}	5.47×10^{-4}
1.005	6.31×10^{-5}	6.39×10^{-5}	6.81×10^{-5}	7.63×10^{-5}	8.16×10^{-5}	9.52×10^{-5}	1.38×10^{-4}	1.94×10^{-4}	7.62×10^{-4}	0.00328
1.01	2.49×10^{-4}	2.52×10^{-4}	2.69×10^{-4}	3.01×10^{-4}	3.22×10^{-4}	3.75×10^{-4}	5.41×10^{-4}	7.61×10^{-4}	0.00294	0.0123
1.02	9.73×10^{-4}	9.85×10^{-4}	0.00105	0.00117	0.00125	0.00146	0.00209	0.00293	0.011	0.0435
1.05	0.00566	0.00572	0.00608	0.00678	0.00723	0.00837	0.0119	0.0163	0.057	0.196
1.1	0.0201	0.0204	0.0216	0.0239	0.0254	0.0293	0.0406	0.0547	0.172	0.502
1.2	0.0648	0.0655	0.069	0.0759	0.0803	0.0911	0.122	0.160	0.430	1.03
1.3	0.119	0.121	0.127	0.138	0.146	0.164	0.214	0.272	0.657	1.39
1.4	0.177	0.178	0.187	0.203	0.212	0.237	0.303	0.377	0.837	1.63
1.7	0.336	0.339	0.351	0.376	0.391	0.428	0.523	0.623	1.16	1.95
2.0	0.463	0.465	0.481	0.509	0.527	0.569	0.674	0.780	1.30	2.00
2.5	0.611	0.614	0.630	0.660	0.679	0.722	0.827	0.927	1.38	1.92
3.0	0.708	0.711	0.726	0.755	0.773	0.814	0.911	1.00	1.38	1.80
4.0	0.820	0.822	0.835	0.861	0.876	0.911	0.992	1.06	1.33	1.60
5.0	0.879	0.881	0.892	0.914	0.927	0.957	1.02	1.08	1.28	1.47
6.0	0.914	0.916	0.926	0.944	0.955	0.981	1.04	1.09	1.25	1.39
7.0	0.936	0.938	0.946	0.963	0.973	0.995	1.04	1.09	1.22	1.33
8.0	0.951	0.953	0.960	0.975	0.984	1.00	1.05	1.08	1.19	1.28
9.0	0.962	0.963	0.970	0.983	0.991	1.01	1.05	1.08	1.18	1.25
10.0	0.970	0.971	0.977	0.989	0.996	1.01	1.05	1.08	1.16	1.22

for near the maximum rotation, $a \approx \pm 0.998$, that can be produced by spinup via accretion from a disk [45].)

(iv) The white dwarf background reduces the maximum detectable black hole mass by about a factor of 2.5, independent of the spin.

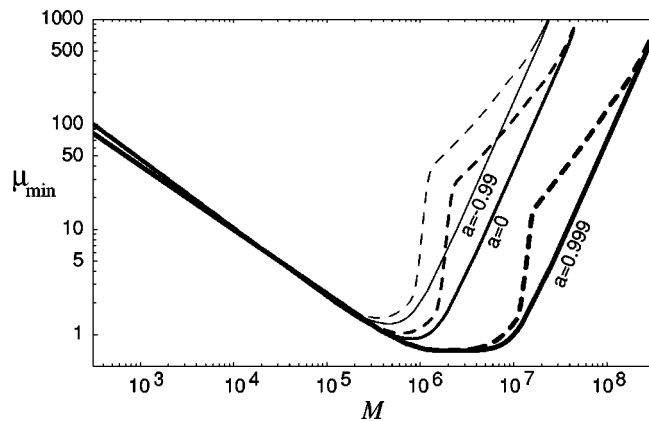


FIG. 1. The minimum mass μ_{min} that the inspiraling object must have in order to produce a signal to noise ratio $S/N > 10$ in its dominant harmonic, $m=2$, during the last year of its inspiral. This μ_{min} is plotted as a function of the black-hole mass M , for various black-hole spin parameters a . The solid curves are for the LISA noise spectrum; the dashed curves are for the LISA noise plus a stochastic background noise due to white-dwarf binaries [44].

(v) The white dwarf background and the black hole spin have little influence on the minimum detectable mass M . This is because, at low M , the object travels a large radial distance in its last year of life, so most of the signal to noise

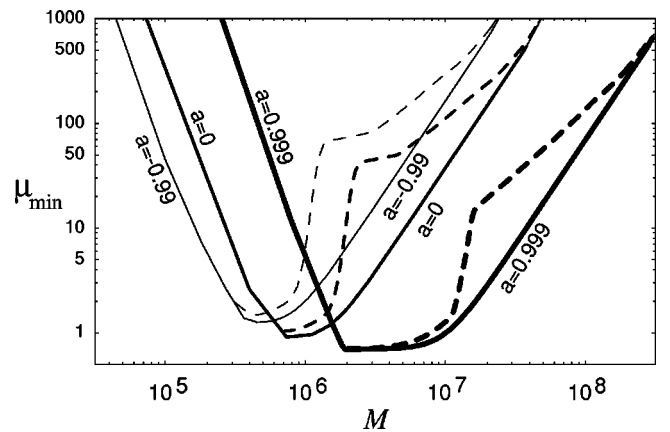


FIG. 2. The minimum mass μ_{min} that the inspiraling object must have in order to produce a signal to noise ratio $S/N > 10$ in its dominant harmonic, $m=2$, during the last year of its inspiral, and in the vicinity of the horizon, $(2/3)f_{2,\text{isco}} < f_2 < f_{2,\text{isco}}$. This μ_{min} is plotted as a function of the black-hole mass M , for various black-hole spin parameters a . The solid curves are for the LISA noise spectrum; the dashed curves are for the LISA noise plus a stochastic background noise due to white-dwarf binaries [44].

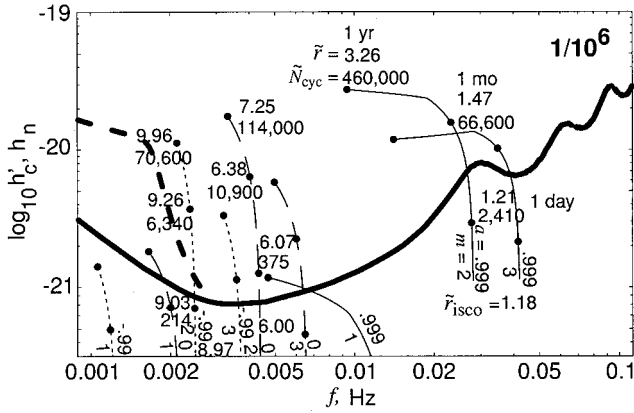


FIG. 3. Gravitational waves from a $1M_{\odot}$ white dwarf or neutron star spiraling into a 10^6M_{\odot} black hole at 1 Gpc distance from Earth, as observed by LISA. The thick solid curve is LISA's rms noise level $h_n(f)$ averaged over the sky; the thick dashed curve is an estimate of the stochastic-background ‘noise’ produced by white dwarf binaries. Each thin curve is the modified characteristic amplitude $h'_c(f)$ for a harmonic of the waves, and is labeled vertically by the hole's spin parameter a and the harmonic number m . The three dots on each curve indicate the waves properties 1 yr (left dot), 1 month (center dot) and 1 day (right dot) before reaching the isco. The dots on the dominant, $m=2$, harmonics are labeled by the orbital radius $\tilde{r}=r/M$ and the number of $m=2$ wave cycles remaining until the isco. The isco radius is shown at the bottom of each $m=2$ curve.

comes from radii $r \gg r_{\text{isco}}$ where the spin is unimportant, and (by virtue of the small M) most comes from frequencies high enough that the white-dwarf background is negligible.

For probing the immediate vicinity of the horizon, we are interested in waves with frequencies, say, $(2/3)f_{2,\text{isco}} < f_2 < f_{2,\text{isco}}$. Figure 2 shows the range of systems for which $(S/N)_{\text{rms}} > 10$ in this frequency band, at a distance $r_o = 1$ Gpc, during the last year of inspiral. Note that restricting attention to this near-horizon frequency range has reduced substantially the set of detectable systems: for $\mu = 10M_{\odot}$, the minimum black-hole mass is increased by a

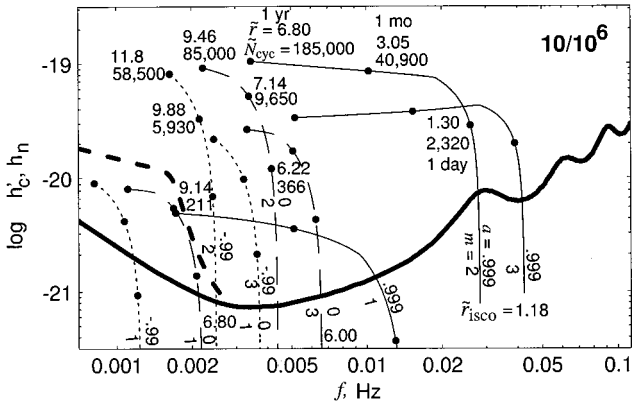


FIG. 4. Gravitational waves from a $10M_{\odot}$ black hole spiraling into a 10^6M_{\odot} black hole at 1 Gpc distance from Earth, as observed by LISA. For notation see the caption of Fig. 3.

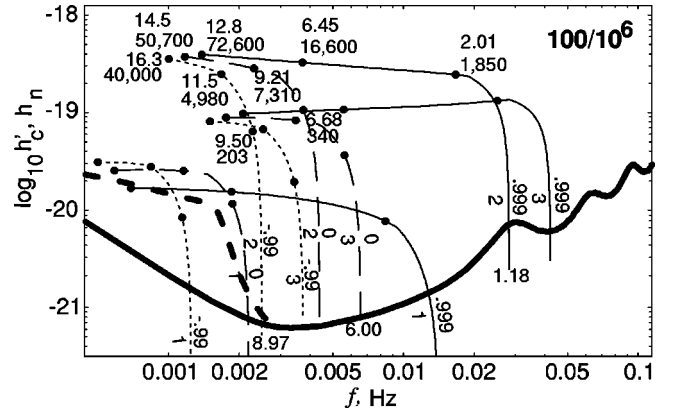


FIG. 5. Gravitational waves from a $100M_{\odot}$ black hole spiraling into a 10^6M_{\odot} black hole at 1 Gpc distance from Earth, as observed by LISA. For notation see the caption of Fig. 3.

factor of ~ 20 – 100 , depending on the spin a . Nevertheless, there is still a wide range of systems accessible for study.

For distances larger than $r_o \sim 1$ Gpc, cosmological effects have a significant influence on the signal [46]. At fixed $\{a, M(1+z), \mu(1+z)\}$ (where z is the cosmological redshift), the characteristic amplitude and signal to noise ratio scale $\propto 1/r_{oL}$, where r_{oL} is the luminosity distance to Earth. The scaling of $(S/N)_{\text{rms}}$ with $\mu(1+z)$ is not so simple, because it influences the waves' frequency evolution in complicated ways that entail the relativistic correction functions. For extremely rough estimates, one can use the leading-order (in $\tilde{\Omega}$) expression for $h_{c,2}$ [Eq. (3.16), $S/N \propto h_{c,2}^2 \propto \mu^{1/2}/r_{oL}$] to infer $\mu_{\text{min}}(1+z) \propto r_{oL}^2$ for the minimum detectable object mass at fixed a and $M(1+z)$, but for reliable results, one must repeat the analysis (sketched above) by which we arrived at Figs. 1 and 2.

C. Evolution of the waves during inspiral

To gain insight into the emitted waves and how they evolve during the inspiral, we have constructed Figs. 3–7. Each figure depicts the waves' evolution for the value of object mass μ and hole mass M (in solar masses) listed in

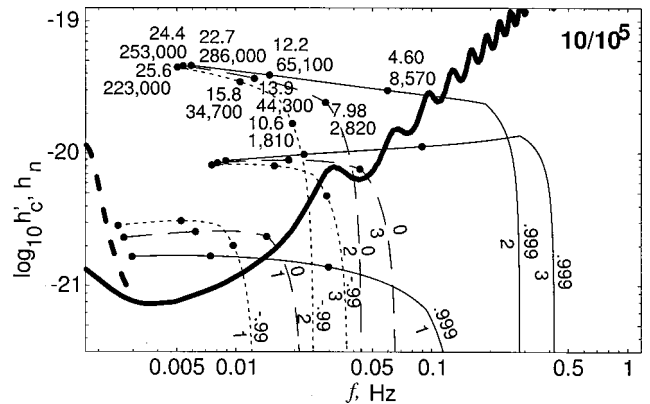


FIG. 6. Gravitational waves from a $10M_{\odot}$ black hole spiraling into a 10^5M_{\odot} black hole at 1 Gpc distance from Earth, as observed by LISA. For notation see the caption of Fig. 3.

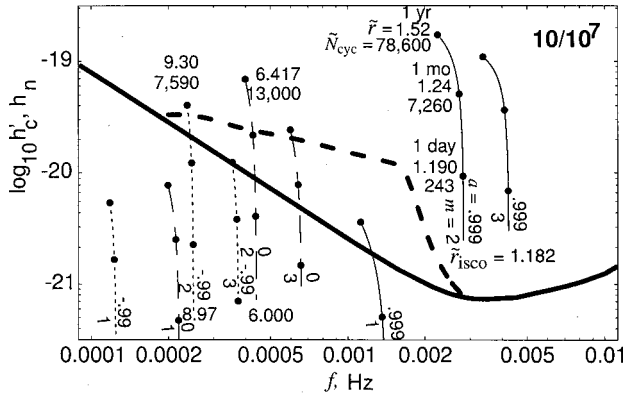


FIG. 7. Gravitational waves from a $10M_{\odot}$ black hole spiraling into a 10^7M_{\odot} black hole at 1 Gpc distance from Earth, as observed by LISA. For notation see the caption of Fig. 3.

bold letters in the upper right corner. The horizontal axis is the waves' frequency f and the vertical axis their modified characteristic amplitude h'_c . As the inspiral proceeds, the waves sweep upward in frequency (left to right) along one of the thin curves. These evolutionary curves are shown for three different values of the black-hole spin, $a = -0.99$ (retrograde orbit, short-dashed curves), $a = 0$ (no rotation, long-dashed curves) and $a = +0.999$ (prograde orbit, solid curves). For each spin, three curves are shown corresponding to the three lowest harmonics $m = 1, 2, 3$ of the orbital frequency. The values of a and m for each evolutionary curve are listed near the vertical end point of the curve. Also shown in each figure is the rms noise amplitude h_n for LISA: a thick solid curve in the absence of a white-dwarf-binary background and a thick dashed curve including that background.

The range of frequency sweep is strongly dependent on the masses μ and M of object and hole. Neglecting the relativistic correction factor \mathcal{T} (which is unimportant for this purpose when the frequency sweep is substantial), Eq. (3.3) tells us that $f_{\text{isco}}/f_{1\text{ yr}} \propto (\mu/M)^{3/8} (1/M)^{3/8}$, where $f_{1\text{ yr}}$ is the frequency 1 yr before reaching the isco. Thus, the greatest frequency sweep is for the least extreme mass ratio and the smallest hole mass, $\mu/M = 10/10^5$ (Fig. 6) with f_2 sweeping from ~ 0.006 Hz to 0.4 Hz, while the smallest sweep is for the most extreme mass ratio and largest hole mass, $\mu/M = 10/10^7$ (Fig. 7), with f_2 sweeping only from ~ 0.0023 to 0.0027 Hz.

The height of a signal curve h'_c above the noise curve h_n is about equal to the signal to noise ratio in an appropriate bandwidth Δf : $\Delta f = f$ well away from the end point of inspiral and $\Delta f = 2(f - f_{\text{isco}})$ near the end point; cf. the discussion of the definition of h'_c at the end of Sec. II. Near the end point of inspiral h'_c plunges for three reasons: (i) because of the narrowing of our chosen bandwidth, (ii) because the rate of frequency sweep speeds up due to flattening of the effective potential for the object's radial motion, and this produces a reduction in the number of cycles N_{cyc} in a given bandwidth and reduction in $h'_c \propto \sqrt{N_{\text{cyc}}}$, and (iii) because, for large a and prograde orbits, the orbit sinks deep into the throat of the hole's embedding diagram, from where waves have difficulty escaping.

On each signal curve there are three solid dots. They label (f, h'_c) for specific times during the inspiral: $T = 1$ yr before the end point (leftmost dot), $T = 1$ month before the end point (center dot), and $T = 1$ day before the end point (right dot). Beside the dots for the dominant harmonic, $m = 2$, are shown two numbers that characterize the orbit and waves at that time: the radius $\tilde{r} = r/M$ of the orbit in units of the black-hole mass and the number of gravitational-wave cycles in the $m = 2$ harmonic, from that time until the end point of inspiral. At the bottom end of each $m = 2$ curve is shown the radius \tilde{r} of the isco.

It is worthwhile to scrutinize the details of these figures, including the numbers beside the dots. Consider, for example, Fig. 4 for a $\mu = 10M_{\odot}$ object (black hole) spiraling into a $M = 10^6M_{\odot}$ hole. If the big hole is rapidly rotating and the orbit is prograde so that $a = +0.999$, then the dominant $m = 2$ evolutionary curve shows the object, 1 yr before its death, at $\tilde{r} = 6.80$ (3.4 Schwarzschild radii), with a signal to noise ratio of $h_c/h_n \sim 100$, and with 185 000 cycles of gravitational waves left until death. One month before death, the object is at $\tilde{r} = 3.05$ (1.53 Schwarzschild radii), with $h_c/h_n \sim 50$, and with 40 000 cycles left. One day before death, it is at $\tilde{r} = 1.30$ (compared to 1.18 for the isco), with $h_c/h_n \sim 10$ and with 2320 cycles left. It is impressive how long the object lingers in the vicinity of the horizon, and how many wave cycles it emits.

For a nonspinning hole $a = 0$, the numbers are less impressive but still remarkable: the last year is spent spiraling from $\tilde{r} = 9.46$ (4.73 Schwarzschild radii) to the isco at $\tilde{r} = 6$ (3 Schwarzschild radii), during which 85 000 wave cycles are emitted and h_c/h_n drops from ~ 100 to ~ 10 at 1 day and then to zero.

The large number of wave cycles carry a large amount of information about the source. We shall discuss this issue in Sec. V D below.

Figures 3–5 illustrate the influence of the mass of the inspiraling object on the signal strength. For M fixed at 10^6M_{\odot} , 1 yr before merger the $m = 2$ signal to noise ratios h_c/h_n are ~ 15 for $\mu = 1M_{\odot}$, ~ 100 for $\mu = 10M_{\odot}$ and ~ 500 for $\mu = 100M_{\odot}$. This is a moderately faster growth than our crude estimate $\propto \mu^{1/2}$ in Sec. V B. Notice that h_c/h_n drops below 10 1 month before the end point for $\mu = 1M_{\odot}$ and 1 day before the end point for $\mu = 10M_{\odot}$.

To maximize the exploration of the horizon's vicinity, we want the object to spend its entire last year at radii $\tilde{r} \lesssim 10$. If the object is a $10M_{\odot}$ hole, this is the case when $M \gtrsim 10^6M_{\odot}$; cf. Figs. 4, 6, and 7. For $M < 10^6M_{\odot}$, such exploration is debilitated by the large frequency sweep; cf. Fig. 6. We have previously met this issue in Sec. V B.

Figure 7 shows that the white-dwarf-binary background is a serious issue for hole masses $M \sim 10^7M_{\odot}$, while Figs. 3–6 show that it is relatively unimportant for $M \lesssim 10^6M_{\odot}$. We have previously met this in Sec. V B.

D. Information carried by the waves

As is well known [47], the waves' highest accuracy information is carried by the time evolution of their phase. For

circular, equatorial orbits, where there is no orbital precession, the phase evolution will be the same for all the harmonics as for the orbit itself, and that phase evolution is embodied in $d\Phi/d \ln \Omega = \Omega^2/\Omega$. Equation (3.2) shows this quantity, at fixed frequency, to be proportional to $\mathcal{N}/M_{\text{chirp}}^2$, where

$$M_{\text{chirp}} = \mu^{1/2} M^{1/3} \quad (5.3)$$

is the system's chirp mass. Since a year of observations will typically entail $N_{\text{cycle}} \sim 10^5$ cycles of waves, and by the method of matched filters one can detect a secular shift of one waveform with respect to another by a small fraction of a cycle [47], the ‘‘raw’’ precision for measuring the evolution of $\mathcal{N}/M_{\text{chirp}}$ will be of order 10^{-6} .

If most of the last year is spent near the horizon, say at frequencies $f/f_{\text{isco}} = \Omega/\Omega_{\text{isco}} \geq 0.1$ (as will usually be the case), then this phase evolution will depend strongly not only on the chirp mass, but also—through the function $\mathcal{N}(f/f_{\text{isco}})$ —on the black-hole spin parameter a .

This strong a dependence is exhibited in Fig. 8. Even for $a < 0.5$, where the curves $\mathcal{N}(f/f_{\text{isco}})$ for different a look very close together, $\partial \mathcal{N}/\partial a \sim 0.1$, this a dependence translates into $\partial N_{\text{cycles}}/\partial a \sim 10^4$, which is huge. Thus, it is reasonable to expect the measured phasing to determine both a and M_{chirp} to high precision—though a detailed parameter study is needed to be absolutely certain.

The absolute frequencies associated with the observed phase evolution (e.g., the measured frequency at the end of inspiral) are determined by a combination of a and the hole's mass M . This absolute frequency scale presumably will be measured much less accurately than the phasing itself, but still, probably, accurately enough to determine the mass M to a very interesting precision. Knowing M_{chirp} , a , and M , one can then compute the object's mass μ ; and from the absolute amplitudes of the waves one can then infer the distance r_o from the system to Earth.

Poisson [48] has estimated the accuracies with which such phase-evolution measurements can determine M , $\eta = \mu/M$, and a . His estimates are based on an analytic model of the signal in which (translated into our notation) \mathcal{N} is expanded

in powers of $\Omega - \Omega_{\text{isco}}$ and only the leading order term is kept. Poisson assumes $M = 10^6 M_\odot$, $\mu = 10 M_\odot$, $a \sim 0$ (i.e., not close to ± 1) and a measurement time of 1 yr. For these parameters, our Figs. 8 and 4 suggest that, for $a \leq 0.5$, Poisson's expansion may be accurate to within a few 10's of percent, but for $a \geq 0.9$ it is seriously inaccurate. His estimated measurement accuracies are $\Delta a \sim 0.05/\rho$, $\Delta M/M \sim 0.002/\rho$, and $\delta \eta/\eta \sim 0.06/\rho$, where ρ is the amplitude signal to noise ratio.

Our Tables VIII and IX for \mathcal{N} and \mathcal{T} (the relativistic corrections to the orbital phase evolution rate $d\Phi/d \ln f$ and the time T to the end of inspiral) can serve as the foundation a more definitive computation of the phasing-based measurement accuracies.

Information is also carried by the relative amplitudes of the waves' harmonics. Most promising, we think, are the amplitude ratios for the first and second harmonics and for the third and second. We plot these ratios in Fig. 9, as parametric functions of the hole's spin a and the orbital radius r/r_{isco} . From this plot it is evident that the instantaneous amplitude ratios will give both a and the instantaneous r/r_{isco} with moderate accuracy—though only for those systems with strong enough signals that the weakest of these harmonics, $m=1$, stands up strongly above the noise; cf. the short-dashed curves in Figs. 3–7.

In our idealized case of circular, equatorial orbits, this harmonic-ratio information is not independent of that from the orbital phasing, but it could provide a confirmation of the phasing conclusions.

In the more realistic case of noncircular, nonequatorial orbits, the waveforms will be much richer and there will be many more parameters to solve for. Our survey of the circular, equatorial case gives some rough indication of the kinds of information one can extract and by what methods.

VI. CONCLUDING REMARKS

In this paper we have tabulated the results of TSN-based computations of the waves emitted by an object spiraling into a spinning, massive black hole on a slowly shrinking,

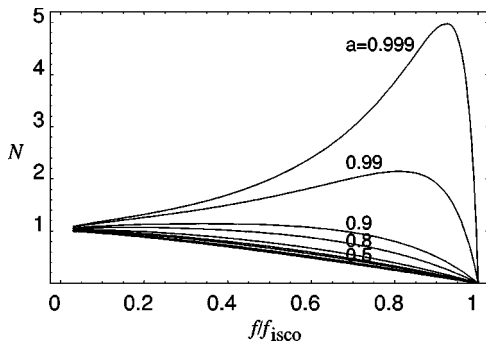


FIG. 8. \mathcal{N} the relativistic correction to $d\Phi/d \ln \Omega = \Omega^2/\Omega$ (the number of radians of orbital inspiral per unit logarithmic change of orbital or gravitational-wave frequency), plotted against $f/f_{\text{isco}} = \Omega/\Omega_{\text{isco}}$ (the ratio of gravitational-wave frequency to the frequency when the isco is reached and the inspiral ends).

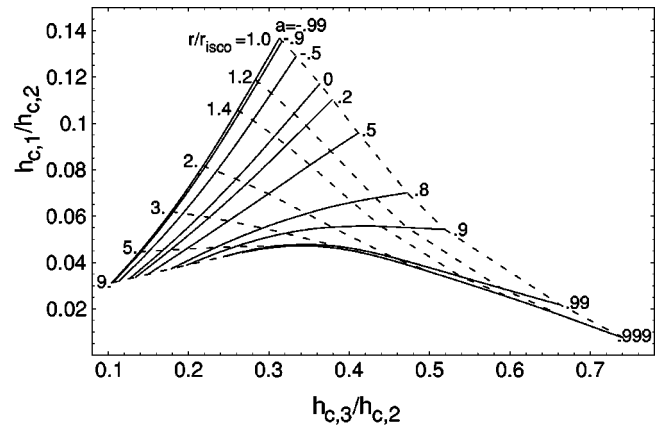


FIG. 9. The ratios $h_{c,1}/h_{c,2}$ and $h_{c,3}/h_{c,2}$ as functions of the black hole spin a and the orbiting object's radius r/r_{isco} .

circular, equatorial orbit. Our Tables II–X can serve as a foundation for future mission-definition studies for LISA—most particularly, for studies of how changes in the mission design may affect LISA’s ability to detect such inspiral waves, for studies of the accuracies with which LISA’s data can extract the properties of the source, and for explorations of possible data analysis algorithms.

Much more important, in the long run, will be the extension of our analysis to nonequatorial and noncircular orbits. This extension is urgent, since models of active galactic nuclei predict, rather firmly, that the orbits will be nonequatorial and quite noncircular, and since the earliest possible date for LISA to fly is less than ten years in the future.

ACKNOWLEDGMENTS

For helpful discussions we thank Fintan Ryan and Eric Poisson. For information and advice about the LISA noise curve we thank John Armstrong, Peter Bender, Curt Cutler, Frank Estabrook, Robin (Tuck) Stebbins, and Massimo Tinto, and we thank Bender and Stebbins for providing us with a table of the noise curve from Ref. [39]. For information and advice about white-dwarf–binary background noise, we thank Peter Bender, Sterl Phinney and Tuck Stebbins. This paper was supported in part by NASA grants NAGW-4274, NAG5-6840 and their predecessors, and in view of its future applications to LIGO, by NSF grants PHY-9800111, PHY-9996213, AST-9731698 and their predecessors.

APPENDIX: NUMERICAL METHODS

Teukolsky [10] found that the equations describing perturbations of the Kerr spacetime could be separated into separate radial and angular equations. For the circular, equatorial orbits studied in this paper, the challenges of solving the perturbation equations are all associated with the numerical solution of the radial equation. We have used Green function methods to solve the radial equation and determine the power radiated down the horizon and to infinity by a particle in a circular equatorial orbit. The general method of solution and formulation of the problem is well described in Ref. [49], and we refer the interested reader there for details. In this appendix we describe several innovations that can dramatically speed the solution of the radial equation compared to the more conventional methods applied elsewhere.

The Teukolsky radial equation is a second order, ordinary differential equation. In the form given originally by Teukolsky [10] the equation is stiff and the solution satisfying the physical boundary conditions is difficult to obtain. Sasaki and Nakamura [11] found, through a local change of variables, a form of the radial equation which is not stiff, and we have worked with the radial equation in that form.

In the Sasaki-Nakamura formulation, the homogeneous (source-free) radial equation takes the form

$$\left[\frac{d}{dr_*} - \mathcal{F}(r_*) \frac{d}{dr_*} - \mathcal{U}(r_*) \right] X = 0. \quad (\text{A1})$$

Here r_* is the so-called tortoise coordinate, which ranges from $-\infty$ at the (outer) horizon to ∞ at spatial infinity. (In

this appendix, and in this appendix only, we express all dimensioned quantities, such as r and r_* , in terms of the black hole’s mass M , eschewing for convenience the superscript-tilde notation used elsewhere in this paper.) The tortoise coordinate can be expressed analytically in terms of the Boyer-Lindquist radial coordinate r and the location of the inner and outer horizons r_+ and r_- :

$$r_* = r + \frac{2}{r_+ - r_-} [r_+ \ln(r - r_+) - r_- \ln(r - r_-)] \quad (\text{A2a})$$

where

$$(r - r_+)(r - r_-) = r^2 - 2r + a^2 \quad \text{and} \quad (\text{A2b})$$

$$r_+ \geq r_-. \quad (\text{A2c})$$

The functions \mathcal{F} and \mathcal{U} are parametrized by the angular frequency of the perturbation $\omega = 2\pi f$, the angular momentum of the spacetime a , and the angular separation constants l and m (with $|m| \leq l$). (For the particular forms of \mathcal{F} and \mathcal{U} see [49].) For circular, equatorial orbits ω is always an integer multiple of the orbital angular frequency, $\omega = \omega_m \equiv m\Omega = 2\pi f_m$.

To obtain the Green function solution to the radial equation with source we need the two solutions to the homogeneous equation corresponding to the physical boundary conditions at infinity (no in-coming radiation) and the horizon (no up-going radiation). These solutions are determined numerically by posing the boundary conditions near infinity or the horizon and integrating the radial equation inward or outward, as appropriate. In the Sasaki-Nakamura variables, obtaining a solution to the radial equation poses no particular challenge; correspondingly, it is conventional to use a “work-horse” integrator (e.g., Runge-Kutta or Bulirsch-Stoer) to solve the equation. On the other hand, the radial equation arises from a separation of variables and is parametrized by the separation constants l , m and ω , corresponding to the resolved angular and temporal dependence of the perturbation. Consequently, it is necessary to solve the radial equation separately for every important set of angular multipoles (l, m) and frequency ω . For very relativistic orbits even moderate accuracy in the total radiated power may require solving the radial equation tens of thousands of times for different angular multipoles and harmonics of the orbital frequency. Consequently, speeding the solution while preserving its accuracy is of fundamental importance. In the remainder of this appendix we address several innovations we have made in solving this equation that, depending on the details of the orbit and the desired accuracy of the solution, can result in a several order of magnitude reduction in the solution time compared to a conventional approach.

1. Boundary conditions at the horizon

As one approaches the horizon, the physical solution for the radial function, corresponding to down-going radiation, leads to the boundary conditions used for the numerical integration of one of the homogeneous solutions of the Sasaki-Nakamura equation:

$$\lim_{r_* \rightarrow -\infty} X_H(r_*) = e^{-i\omega r_*}, \quad (\text{A3a})$$

$$\lim_{r_* \rightarrow -\infty} \frac{dX_H}{dr_*}(r_*) = -i\omega_- e^{-i\omega_- r_*}, \quad (\text{A3b})$$

where

$$\omega_- = \omega - \frac{am}{2r_+} \quad (\text{A3c})$$

and r_+ is the radius of the outer horizon in Boyer-Lindquist coordinates.

As a practical matter the boundary conditions used to determine X_H are posed at some large, negative but finite r_* , say R_*^* ; i.e., ‘‘close to,’’ but not at, the horizon. Using Eqs. (A3) evaluated at finite R_*^* for the boundary conditions introduces fractional errors of order $\delta = r - r_+$ into the solution. This error can be represented as an error in the amplitude of the power radiated down the horizon and the introduction of some small component of radiation up-going from the horizon. These errors propagate to large r_* where they contribute to the out-going radiation and lead to errors in the calculated power radiated to infinity by the orbiting particle.

The errors introduced by using Eqs. (A3) when posing boundary conditions at finite radius can be expressed as a power series in δ . The coefficients of that expansion can be estimated by solving the equations several times, for different R_*^* , and using Richardson extrapolation. To estimate the first N terms in the error expansion requires $N+1$ numerical solutions of the equations, each beginning with the boundary conditions posed at a different R_*^* . Controlling the error requires that the radial equation be solved at least twice and often three or more times at different, large $|R_*^*|$.

To improve the convergence rate of this error estimate and allow us to pose our boundary conditions at smaller $|R_*^*|$ we have solved the Sasaki-Nakamura equation analytically about the point at $r_* = -\infty$, finding the first corrections in δ to the boundary conditions given by Eqs. (A3). The improved boundary conditions are given by

$$X_H(r_*) = (1 + \delta A') e^{-i\omega_- r_*}, \quad (\text{A4a})$$

$$\frac{dX_H}{dr_*}(r_*) = \left[-i\omega_-(1 + \delta A') + \frac{\delta d}{2r_+} A' \right] e^{-i\omega_- r_*}, \quad (\text{A4b})$$

where

$$A' = \left[\mathcal{F}^{(1)} + \frac{d}{4r_+^2} (U_2^{(1)} + F_1^{(1)} + G_1^{(1)}) \right] \times \left[\frac{d^2}{4r_+^2} + i\epsilon \frac{d}{r_+} \omega_- \right]^{-1}, \quad (\text{A4c})$$

$$\delta \equiv r - r_+, \quad (\text{A4d})$$

$$d \equiv r_+ - r_-, \quad (\text{A4e})$$

$$\mathcal{F}^{(1)} \equiv -i\omega_- \frac{d}{2r_+}, \quad (\text{A4f})$$

$$U_2^{(1)} \equiv \lambda + \frac{4r_-}{r_+} - 2r_+ \omega_- \left(\frac{2(2+d)}{d} - \frac{2r_+}{d^2} \omega_- \right) - \left(1 - \frac{d(2+d)}{r_+} \right) \frac{4r_+^2}{d^2} \omega_-^2, \quad (\text{A4g})$$

$$F^{(1)} \equiv 2ir_+ \omega_- F(0), \quad (\text{A4h})$$

$$G_1^{(1)} \equiv -2 + d/2, \quad (\text{A4i})$$

$$F(0) \equiv \gamma'(r_+)/\gamma(r_+), \quad (\text{A4j})$$

$$\gamma(r) \equiv \sum_{k=0}^4 \gamma_k r^{-k}, \quad (\text{A4k})$$

$$\gamma_0 \equiv \lambda(\lambda+2) - 12a\omega(a\omega-m) - 12i\omega, \quad (\text{A4l})$$

$$\gamma_1 \equiv 8i[3a^2\omega - a\lambda(a\omega-m)], \quad (\text{A4m})$$

$$\gamma_2 \equiv 12[-2ai(a\omega-m) + a^2 - 2a^2(a\omega-m)^2], \quad (\text{A4n})$$

$$\gamma_3 \equiv 24a^2[-1 + ia(a\omega-m)], \quad (\text{A4o})$$

$$\gamma_4 \equiv 12a^4, \quad (\text{A4p})$$

$$\lambda \equiv l(l+1) - 2am\omega + a^2\omega^2 + 2. \quad (\text{A4q})$$

The numerical solution to the radial equation using these improved boundary conditions converges upon the true solution more quickly than a solution using the boundary conditions (A3). We are thus able to pose approximate horizon boundary conditions at smaller $|R_*^*|$, reducing the domain over which we must integrate the radial equation and, often, the number of times we must integrate the equation for each (ω, l, m) in order to obtain a solution of controlled accuracy.

2. Boundary conditions at spatial infinity

As $r_* \rightarrow \infty$, the physical solution for the radial function, corresponding to no in-going radiation, leads to the boundary conditions for the numerical integration of the other critical solution of the radial equation:

$$\lim_{r_* \rightarrow \infty} X_\infty = e^{i\omega r_*}, \quad (\text{A5})$$

$$\lim_{r_* \rightarrow \infty} \frac{dX_\infty}{dr_*} = i\omega e^{i\omega r_*}. \quad (\text{A6})$$

As with the boundary conditions at the horizon, we construct the solution X_∞ beginning with boundary conditions posed at finite R_*^* , not at infinity. Using the asymptotic form of the boundary conditions to set X and X' at finite radius leads to errors of fractional order $1/R_*^*$ in the solution, which can be represented as an error in the amplitude of the out-going radiation and the introduction of some small in-going radiation component. These lead, in turn, to errors in the estimated power radiated to infinity and down the hori-

zon. We can use Richardson extrapolation to estimate and reduce this error; however, as before, the radiated power must be determined at several different large R_+^* in order to estimate and reduce the error.

To permit a more accurate estimate of the radiated power from X and X' evaluated at smaller R_+^* we have solved the Sasaki-Nakamura equation analytically about the point at $r_* = \infty$, finding the first corrections in $1/R_+^*$ to the asymptotic form of the radial function X . For finite R_+^* we have

$$X_\infty(r_*) = \left(1 + \frac{a_1}{r}\right) e^{i\omega r_*}, \quad (\text{A7a})$$

$$\frac{dX_\infty}{dr_*}(r_*) = i\omega \left(1 + \frac{a_1}{r}\right) e^{i\omega r_*}, \quad (\text{A7b})$$

where

$$a_1 = \frac{\gamma_1}{\gamma_0} + \frac{i}{2} \left[\omega(a^2 + 4) + 2am + \frac{\lambda + 2}{\omega} \right]. \quad (\text{A7c})$$

We use these expressions, evaluated at finite but large R_+^* , to set the boundary condition for the numerical solution of the homogeneous radial equation. We continue to use Richardson extrapolation to control the error of the solutions; however, each step in the extrapolation has a greater effect on the error and the extrapolation can take place at smaller R_+^* .

3. A more suitable choice of variables

The solution X to the Sasaki-Nakamura equations is a complex oscillatory function. Integrating the equations directly for X requires a spatial resolution Δr_* less than the local wavelength of X ,

$$\Delta r_* \lesssim \left| \frac{d \ln X}{dr_*} \right|^{-1}. \quad (\text{A8})$$

When solving for the radial function corresponding to a high temporal frequency $|\omega|$ the step-size can become quite small, with a corresponding increase in the computational time for an accurate solution.

It is advantageous in circumstances like these to reformulate the problem in action-angle variables, whose variation is both slower and smoother than the variations in X . Writing X as

$$X \equiv \exp[i\Phi(r_*)] \quad (\text{A9a})$$

we define the two real functions ξ and ϕ as the imaginary and real parts of Φ :

$$\xi \equiv \Re(\Phi) \quad (\text{A9b})$$

$$\phi \equiv \Im(\Phi). \quad (\text{A9c})$$

With this substitution the linear Sasaki-Nakamura equation for complex X becomes a pair of coupled non-linear equations for the real ξ and ϕ . The equation for ξ is second order while the equation for ϕ can be integrated immediately to obtain a first order equation. (This is expected since the solution for X is determined only up to an overall phase.) Both ϕ and ξ vary slowly and smoothly compared to X . This is particularly true as one moves toward either the horizon or spatial infinity, where X is oscillatory in r_* while ξ is constant and ϕ is linear. Correspondingly, the numerical solution of the equations for ϕ and ξ require much less resolution for the same numerical accuracy, dramatically speeding the integration of the radial equation.

4. Numerical solution of the equations for ξ and ϕ

The local errors committed by, e.g., a fourth order Runge-Kutta integration of the radial equation are proportional to Δr_* [5]. Reducing the step-size and increasing the number of integration steps will decrease the overall solution error algebraically, i.e., as a fixed power of Δr_* , while increasing the time required for a solution. A higher order computational method will increase the solution accuracy more rapidly. *Exponential* convergence of the solution with Δr_* can be obtained if the equations are solved via collocation pseudo-spectral techniques [50]. In a collocation pseudo-spectral method the solution for the dependent variable is approximated as a sum over a suitable set of basis functions. The differential equations, evaluated on the approximate solution at a fixed number of points, then determine the coefficients in the expansion. For problems with smooth solutions the solution accuracy increases exponentially with the number of terms in the approximation (and, correspondingly, with the number of evaluations of the differential equation, which is the analog of the spatial resolution of the integration). Our final innovation is to solve the radial equation using pseudo-spectral techniques. We have chosen a Chebyshev expansion for ξ and ϕ with Gauss-Lobatto collocation points. Our experience is that the best performance is obtained if the integration domain $[R_+, R_-]$ is divided into two parts, at approximately the peak of the effective potential R_0 : i.e., we use two expansions for ϕ and ξ , one in the domain $[R_+, R_0]$ and the other in the domain $[R_0, R_-]$. At R_0 we insist that the two solutions for ϕ and ξ agree in value, and that the solutions for ξ agree also in their first derivative, as is appropriate for functions described by first order and second order differential equations, respectively.

[1] For details of the LIGO/VIRGO network see the web sites <http://www.ligo.caltech.edu/> and <http://www.pg.infn.it/virgo/>.

[2] For details of the LISA mission see <http://lisa.jpl.nasa.gov/> and <http://www.estec.esa.nl/spdwww/future/html/lisa.htm>. For compilations of articles related to LISA see *Proceedings of the*

First International LISA Symposium [Class. Quantum Grav. **14**, 1397 (1997)]; *Laser Interferometer Space Antenna*, edited by William M. Folkner, AIP Conf. Proc. No. 456 (AIP, New York, 1998).

[3] S. Sigurdsson and M. J. Rees, Mon. Not. R. Astron. Soc. **284**,

- 318 (1997).
- [4] S. Sigurdsson, *Class. Quantum Grav.* **14**, 1425 (1997).
- [5] E. S. Phinney (the head of NASA's Mission Definition Team for LISA) has summarized its scientific payoffs at <http://www.cco.caltech.edu/~esp/lisa/lisatab.html>.
- [6] F. D. Ryan, *Phys. Rev. D* **52**, 5707 (1995).
- [7] F. D. Ryan, *Phys. Rev. D* **56**, 1845 (1997).
- [8] T. D. Lee and Y. Pang, *Phys. Rep.* **221**, 251 (1992).
- [9] S. K. Chakrabarti, *Astrophys. J.* **411**, 610 (1996); *Phys. Rev. D* **53**, 2901 (1996); D. Molteni, G. Gerardi, and S. K. Chakrabarti, *Astrophys. J.* **436**, 249 (1994).
- [10] S. A. Teukolsky, *Astrophys. J.* **185**, 635 (1973).
- [11] M. Sasaki and T. Nakamura, *Prog. Theor. Phys.* **67**, 1788 (1982).
- [12] R. Narayan, *Astrophys. J.* **536**, 663 (2000).
- [13] B. Carter, *Phys. Rev.* **174**, 1559 (1968).
- [14] Y. Mino, M. Sasaki, and T. Tanaka, *Phys. Rev. D* **55**, 3457 (1997).
- [15] T. C. Quinn and R. M. Wald, *Phys. Rev. D* **56**, 3381 (1997).
- [16] See, e.g., L. Barack and A. Ori, *Phys. Rev. D* **61**, 061502(R) (2000); L. M. Burko, *Phys. Rev. Lett.* **84**, 4529 (2000); A. G. Wiseman, *Phys. Rev. D* **61**, 084014 (2000); Y. Mino and H. Nakano, *Prog. Theor. Phys.* **100**, 507 (1998).
- [17] T. Tanaka, M. Shibata, M. Sasaki, H. Tagoshi, and T. Nakamura, *Prog. Theor. Phys.* **90**, 65 (1993).
- [18] Y. Mino, M. Sasaki, M. Shibata, H. Tagoshi, and T. Tanaka, *Suppl. Prog. Theor. Phys.* **128**, 1 (1998).
- [19] C. Cutler, D. Kennefick, and E. Poisson, *Phys. Rev. D* **50**, 3816 (1994).
- [20] D. Kennefick, *Phys. Rev. D* **58**, 064012 (1998).
- [21] D. Hils and P. L. Bender, *Astrophys. J. Lett.* **445**, L7 (1995); and unpublished research.
- [22] A. Ori and K. S. Thorne, following paper, *Phys. Rev. D* **62**, 124022 (2000).
- [23] M. Shibata, *Phys. Rev. D* **50**, 6297 (1994).
- [24] See the review by T. Nakamura, K. Oohara, and Y. Kojima, *Suppl. Prog. Theor. Phys.* **90**, 1 (1987).
- [25] D. Kennefick and A. Ori, *Phys. Rev. D* **53**, 4319 (1996).
- [26] F. D. Ryan, *Phys. Rev. D* **53**, 3064 (1996).
- [27] Y. Mino, Ph.D. thesis, Kyoto University (1996).
- [28] S. A. Hughes, *Phys. Rev. D* **61**, 084004 (2000); S. A. Hughes, in *Proceedings of the Third Edoardo Amaldi Meeting on Gravitational Waves*, edited by S. Meshkov (AIP, New York, in press); gr-qc/9912031.
- [29] M. Shibata, *Prog. Theor. Phys.* **90**, 595 (1993).
- [30] M. Shibata, M. Sasaki, H. Tagoshi, and T. Tanaka, *Phys. Rev. D* **51**, 1646 (1995).
- [31] S. L. Detweiler, *Astrophys. J.* **225**, 687 (1978).
- [32] J. M. Bardeen, W. H. Press, and S. A. Teukolsky, *Astrophys. J.* **178**, 347 (1972).
- [33] K. S. Thorne, in *300 Years of Gravitation*, edited by S. W. Hawking and W. Israel (Cambridge University Press, Cambridge, England, 1987), p. 330.
- [34] This definition of $h_{c,m}$ is due to E. E. Flanagan and S. L. Hughes, *Phys. Rev. D* **57**, 4535 (1998). It differs from that used previously by one of the authors [33], in such a way as to free it from dependence on the shape of the detector's noise spectral density $S_h(f)$.
- [35] C. W. Misner, K. S. Thorne, and J. A. Wheeler, *Gravitation* (Freeman, San Francisco, 1973).
- [36] K. S. Thorne, *Rev. Mod. Phys.* **52**, 299 (1980).
- [37] I. D. Novikov and K. S. Thorne, in *Black Holes*, edited by C. DeWitt and B. S. DeWitt (Gordon and Breach, New York, 1973).
- [38] LISA Study Team, *LISA: Laser Interferometer Space Antenna for the detection and observation of gravitational waves, Pre-Phase A Report*, 2nd ed. (Max Planck Institut für Quantenoptik, Garching, Germany, 1998).
- [39] LISA Mission Definition Team (NASA) and LISA Science Study Team (ESA), *LISA: Laser Interferometer Space Antenna* (March Press, Boulder, CO, 1999). The figure on p. 6 of this document shows $h_{\text{SN5,1 yr}}^{\text{SA}}(f)$ as computed by Peter Bender and Robin Stebbins from the LISA error budgets (Tables 4.1 and 4.2 of Ref. [38]), using the transfer function computed by Schilling [41]. Bender and Stebbins kindly provided us with a table of this $h_{\text{SN5,1 yr}}^{\text{SA}}(f)$, from which we computed $h_n(f)$ using Eq. (5.1).
- [40] F. B. Estabrook, M. Tinto, and J. W. Armstrong, *Phys. Rev. D* **62**, 042002 (2000). This paper and an earlier one by the same authors [*Astrophys. J.* **527**, 814 (1999)] develop promising new methods for combining the data from LISA's six light paths so as to remove various kinds of noise, including that of laser frequency fluctuations. Armstrong, Estabrook, and Wu compute $h_{\text{SN5,1 yr}}^{\text{SA}}(f)$ independently of Bender and Stebbins, using the same LISA error budgets [38] but their own version of the transfer function; see Fig. 3 of the *Phys. Rev. D* paper, which agrees to within about 10% with Bender and Stebbins' $h_{\text{SN5,1 yr}}^{\text{SA}}(f)$.
- [41] R. Schilling, *Class. Quantum Grav.* **14**, 1513 (1997). The noise curve plotted in Fig. 5(b) of this paper was based on an error budget which preceded that in Ref. [38], and so differs some from the noise curves in Refs. [39] and [40], especially at low frequencies.
- [42] Figure 5 of D. Hils and P. L. Bender, *Astrophys. J.* **537**, 334 (2000).
- [43] R. F. Webbink and Z. Han, in *Laser Interferometer Space Antenna* [2], p. 61. Figure 2 shows their estimate of $\sqrt{S_h^{\text{SA}}(f)}$. When the Hils-Bender [42] Fig. 5 for $h_{\text{SN5,1 yr}}^{\text{SA}}$ is converted to $h_h^{\text{SA}}(f)$ via $h_{\text{SN5,1 yr}}^{\text{SA}} = 5\sqrt{S_h^{\text{SA}}}\Delta f$ with $\Delta f = 1/1$ yr, it falls between the lowest Webbink-Han estimate ("no wind enhancement" curve) and the highest ("standard model") and agrees to within a factor 2 with both—except for one issue: Webbink and Han do not take account of the cutoff in the noise due to the line spikes of individual white-dwarf binaries ceasing to overlap each other, for 1 yr of integration, at frequencies above about 0.0017 Hz, so their noise curves fail to plunge above there.
- [44] In the computations underlying Figs. 1 and 2 we used the following analytic fit to Bender and Stebbins' [39] LISA noise curve $h_{\text{SN5,1 yr}}^{\text{SA}}(f)$, in which f is measured in Hz:
- $$\sqrt{4.85 \times 10^{-57}/f^4 + 8.38 \times 10^{-47} + 4.85 \times 10^{-43}f^2}.$$
- [45] K. S. Thorne, *Astrophys. J.* **191**, 507 (1974).
- [46] L. S. Finn, *Phys. Rev. D* **53**, 2878 (1996).
- [47] C. Cutler, T. A. Apostolatos, L. Bildsten, L. S. Finn, E. E. Flanagan, D. Kennefick, D. M. Markovic, A. Ori, E. Poisson, G. J. Sussman, and K. S. Thorne, *Phys. Rev. Lett.* **70**, 2984 (1993).
- [48] E. Poisson, *Phys. Rev. D* **57**, 5287 (1998).
- [49] S. A. Hughes, *Phys. Rev. D* **61**, 084004 (2000).
- [50] D. Gottlieb and S. A. Orszag, *Numerical Analysis of Spectral Methods: Theory and Applications* (SIAM, 1977).